ATLAS CONF Note

ATLAS-CONF-2020-024

28th July 2020

Measurement of the production cross section of isolated photon pairs in pp collisions at 13 TeV with the ATLAS detector

The ATLAS Collaboration

A measurement of prompt photon-pair production in proton-proton collisions at $\sqrt{s} = 13$ TeV is presented. The data were recorded by the ATLAS detector at the LHC with an integrated luminosity of 139 fb^{-1}. Events with two photons in the well-instrumented region of the detector are selected, and the photons are required to be isolated and have $E_{\mathrm{T},\gamma_{1(2)}} > 40\,(30)$ GeV for the leading (sub-leading) photon. The differential cross section as functions of several observables for the diphoton system are measured in the fiducial volume and compared to theoretical predictions from state-of-the-art Monte Carlo and fixed-order calculations. The measured integrated cross section is compatible with the predictions from next-to-next-to-leading order and multileg-merged calculations. Predictions from lower-orders in perturbative QCD fail to agree with data within their estimated theoretical uncertainties. Agreement between measured differential cross sections and the most accurate predictions is generally good where expected, showing a clear necessity to take higher-order perturbative QCD corrections into account.

ATLAS-CONF-2020-024
30 July 2020

1 Introduction

The production of a prompt-photon pair in proton-proton collisions is one of the cornerstone processes of the LHC physics program. Most prominently, it is vital for searching for and studying the properties of resonances decaying into photon pairs, such as the Higgs boson or other neutral particles. The main background to resonant diphoton production originates from the continuum production of such pairs, which is the subject of this note. Despite the electromagnetic nature of this process, diphoton production in hadron colliders involves strong-interaction dynamics; theoretical predictions are therefore highly non-trivial and measurements are necessary to scrutinise and validate such predictions.

Prompt photons are those not produced in hadron decays. Non-resonant photons can be produced by various mechanisms in pp collisions at the LHC. In a theoretical or Monte Carlo (MC) picture, prompt photons are typically subdivided into two different production mechanisms: the "direct" production mode, represented by a $q\bar{q} \to \gamma\gamma$ t-channel diagram at leading order; and the "fragmentation" component with a hard γ+jet or dijet configuration and subleading photon emissions in a resummed approach. A schematic representation exemplifies these photon production mechanisms in Fig. 1(a) and Fig. 1(b), respectively. By far the most abundant source of photons in pp collisions are hadron decays like $\pi^0 \to \gamma\gamma$, cf. Fig. 1(c). These are explicitly not the focus of this note and are in fact considered as background. To suppress the contribution of photons from hadron decays (non-prompt), photons are required to be isolated from hadronic activity in their vicinity.

In this analysis the diphoton production at the LHC in pp collisions at $\sqrt{s}$ = 13 TeV is measured with the full Run-2 dataset. Previous diphoton cross section measurements have been performed at 7 TeV by CMS [1, 2] and ATLAS [3, 4], and at 8 TeV by ATLAS [5]. Other prompt-photon measurements have studied single photon production in CMS [6] and in ATLAS [7–11] at $\sqrt{s}$ = 13 TeV.

The main challenge and source of uncertainty on the experimental side is the estimation of the background from non-prompt photons in jet events. In this analysis, a sophisticated background decomposition fit is used to estimate the background contributions using a data-driven technique. The background-subtracted yield is then corrected for detector effects using an iterative unfolding procedure. Differential cross section measurements are presented in a fiducial region as functions of several kinematic observables of the photon pair. State-of-the-art theoretical predictions from fixed-order calculations and from MC event generators are compared to the data.

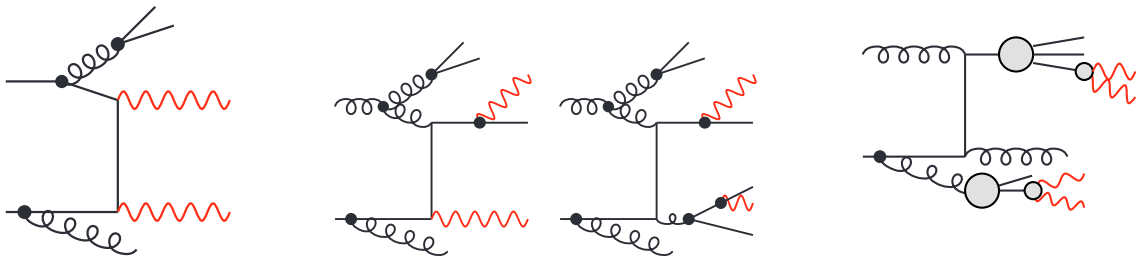

(a) Direct photons (b) Single and double fragmentation photons (c) Non-prompt photons

Figure 1: Schematic of theoretical photon pair production mechanisms. The black dots represent resummed Bremsstrahlung e.g. from a fragmentation function or parton shower, while the grey circles represent hadronisation and hadron decay processes.

2 ATLAS detector

The ATLAS experiment [12] at the LHC is a multi-purpose particle detector with a forward-backward symmetric cylindrical geometry and a near 4π coverage in solid angle.[1] It consists of an inner tracking detector surrounded by a thin superconducting solenoid providing a 2 T axial magnetic field, electromagnetic and hadron calorimeters, and a muon spectrometer.

The inner tracking detector covers the pseudorapidity range $|\eta| < 2.5$. It consists of silicon pixel, silicon microstrip, and transition radiation tracking detectors.

The calorimeter system covers the pseudorapidity range $|\eta| < 4.9$. Within the region $|\eta| < 3.2$, electromagnetic (EM) calorimetry is provided by barrel and endcap high-granularity lead/liquid-argon (LAr) calorimeters, with an additional thin LAr presampler covering $|\eta| < 1.8$, to correct for energy loss in material upstream of the calorimeters. Hadronic calorimetry is provided by the steel/scintillating-tile calorimeter, segmented into three barrel structures within $|\eta| < 1.7$, and two copper/LAr hadronic endcap calorimeters. The solid angle coverage is completed with forward copper/LAr and tungsten/LAr calorimeter modules optimised for electromagnetic and hadronic measurements respectively.

The muon spectrometer surrounds the calorimeters and is based on three large air-core toroidal superconducting magnets with eight coils each. The field integral of the toroids ranges between 2.0 and 6.0 T m across most of the detector. The muon spectrometer includes a system of precision tracking chambers and fast detectors for triggering.

A two-level trigger system is used to select events. The first-level trigger is implemented in hardware and uses a subset of the detector information to reduce the accepted rate to at most nearly 100 kHz. This is followed by a software-based trigger that reduces the accepted event rate to 1 kHz on average depending on the data-taking conditions [13].

3 Data and simulated samples

3.1 Data samples

The data used in this measurement were recorded by the ATLAS detector in pp collisions at $\sqrt{s} = 13$ TeV during the LHC Run-2 data taking period. Events were selected using a diphoton trigger requiring the presence in the EM calorimeter of two clusters of energy depositions with transverse energy above 35 GeV and 25 GeV for the leading and subleading clusters, respectively. Only events taken during stable beam conditions and satisfying detector and data-quality requirements [14] are considered. These requirements ensure that the calorimeters and inner tracking detectors are in nominal operation.

The total integrated luminosity of the collected sample after trigger and data quality requirements amounts to 139 fb^{-1}. Multiple pp interactions (pile-up) can occur in the same bunch crossing, with 34 simultaneous interactions produced on average. The efficiency of the diphoton triggers with respect to the offline selection

[1] ATLAS uses a right-handed coordinate system with its origin at the nominal interaction point (IP) in the centre of the detector and the z-axis along the beam pipe. The x-axis points from the IP to the centre of the LHC ring, and the y-axis points upwards. Cylindrical coordinates (r, ϕ) are used in the transverse plane, ϕ being the azimuthal angle around the z-axis. The pseudorapidity is defined in terms of the polar angle θ as $\eta = -\ln\tan(\theta/2)$. Angular distance is measured in units of $\Delta R \equiv \sqrt{(\Delta\eta)^2 + (\Delta\phi)^2}$.

presented in the next section ranges between 96% and 100% [15] as a function of the transverse energy (E_{T}) of the sub-leading photon.

3.2 Simulated event samples for signal and background processes

Samples of events from a MC simulation are used for the subtraction of subdominant background as well as for cross checks of the subtraction of the dominant background, for the unfolding of detector effects, and as theoretical predictions in the final comparison to the measured data.

All simulated event samples include pile-up effects, as well as the effect on the detector response due to interactions from bunch crossings before or after the one containing the hard interaction. Pile-up interactions deteriorate the resolution of the calorimetric variables. The MC samples are reweighted to match the pile-up noise in data events. All samples were processed through the ATLAS detector simulation based on GEANT4 [16] using the same reconstruction algorithms as used in data.

Diphoton signal samples. Simulated samples of prompt diphoton production were generated with two different programs, SHERPA [17] and PYTHIA8 [18]. The nominal samples used in the analysis are simulated with the SHERPA v2.2 generator [17]. Their size amounts to approximately twice the equivalent luminosity of data. In this setup, matrix elements for $pp \to \gamma\gamma + 0, 1j$[2] at next-to-leading order (NLO) accuracy in the strong coupling constant α_s and $pp \to \gamma\gamma + 2, 3j$ at leading-order (LO) accuracy are matched and merged with the SHERPA parton shower based on Catani-Seymour dipoles [19, 20] using the MEPS@NLO prescription [21, 22]. The virtual QCD correction for matrix elements at NLO accuracy is provided by the OPENLOOPS library [23, 24]. Samples were generated using the NNPDF3.0 next-to-next-to-leading order (NNLO) set [25] of parton distribution functions (PDF), along with the dedicated set of tuned parton-shower parameters developed by the SHERPA authors. Both the direct and fragmentation component of isolated photon production are included by setting the merging scale dynamically in the scheme of Ref. [26], and a photon isolation requirement based on a smooth cone [27] is used with $n = 2$, $\delta = 0.1$ and $\varepsilon = 0.1$. In addition, the loop-induced $gg \to \gamma\gamma$ box process is included in these samples at LO accuracy.

An alternative signal sample was generated with PYTHIA8. Direct production was simulated using LO matrix elements for $pp \to \gamma\gamma$ and showered in PYTHIA8 v8.186 [18] using the NNPDF2.3 LO [28] PDF set with the A14 shower tune [29]. The same framework was used to generate the single-fragmentation component based on LO matrix elements for $pp \to \gamma j$ with one additional photon produced in the parton shower, and the double-fragmentation component based on LO matrix elements for $pp \to jj$ with both additional photons produced in the parton shower. No photon isolation requirement is applied in these samples at the generator level.

Electron background sources. Since electrons can fake photons or even radiate real photons, background processes with prompt electron production from Drell-Yan processes, $Z/\gamma^*(\to ee)$ and $W(\to e\nu)$, are considered and estimated from MC simulation. The samples used to estimate these backgrounds were generated using Powheg-Box v2 [30, 31] interfaced to the PYTHIA8 v8.186 [18] parton shower model with the AZNLO set of tuned parameters [32]. Photos++ 3.52 [33] was used for QED emissions from electroweak vertices and charged leptons. The W/Z samples are normalised to NNLO cross sections calculated with FEWZ [34]. Even though the impact is negligible, a poor modelling of the $p_{\mathrm{T}}(Z)$ spectrum

[2] Here and in the following, j refers to "jet", which at matrix-element level corresponds to a quark or gluon.

in the $Z(\rightarrow ee)$ sample is corrected for using data/MC correction factors from the measurement in Ref. [35].

γj background. While this background is determined in a data-driven approach, SHERPA v2.2 [17] simulations of the $pp \rightarrow \gamma + 1, 2j$@NLO+$3, 4j$@LO process are used for cross checks. The setup is otherwise equivalent to the diphoton signal samples described above.

4 Data selection and observables definition

The photon and event selections are explained in Sections 4.1 and 4.2, respectively, and the definition of the observables is included in Section 4.3.

4.1 Photon reconstruction and selection

Photon candidates are reconstructed from a cluster of energy depositions in the electromagnetic calorimeter [36, 37]. The photon energy is calibrated as described in Ref. [38], and its uncertainty depends on the E_{T} and η of the photon, with a value of $0.2\% - 0.4\%$ for central photons with transverse energy in the intermediate range dominating this analysis. Photons which undergo conversion in the inner detector are distinguished from unconverted photons by associating inner detector tracks to the photon and have generally a lower energy scale uncertainty.

The momenta of the photon candidates are corrected for the position of their associated reconstructed primary interaction vertex. The associated vertex is chosen among all reconstructed vertices, which are required to have at least two inner detector tracks assigned with transverse momentum $(p_{\mathrm{T}}) > 0.5\,\mathrm{GeV}$. The measured trajectories of the two photons, along with the reconstructed vertex information in the event, are used as inputs to a neural-network algorithm trained on simulation to select the most probable primary vertex [39, 40] for the photon candidates.

The identification of photons is based on multiple variables that quantify the longitudinal and lateral shape of the electromagnetic shower produced by the photon. Requirements on these shower-variables are used to identify photons. A detailed description of all variables and selections for the 'tight' photon identification used in this analysis is given in Ref. [41]. The identification variables f_{side} (energy fraction outside of core cells) and w_{s3} (lateral shower width) are used to define control regions. These variables use information in the finely segmented first layer of the electromagnetic calorimeter and are sensitive to differences between candidates from prompt photons and background candidates e.g. from the two collimated photons of a neutral hadron decay. If the photon candidate fails the requirement on at least one of these two variables but passes all other selections of the 'tight' photon identification, it enters into one of the control regions enriched in candidates from non-prompt photons.

The isolation measurement is based on calorimeter information [41]. The initial isolation variable is defined as the sum of the transverse energy computed from topological clusters of calorimeter cells [42] in a cone of $\Delta R = 0.2$ around the photon candidate direction. The transverse energy deposited in the rectangular window around the photon candidate and the expected transverse energy leaking out of this core region into the isolation cone are subtracted from the initial transverse isolation energy. Furthermore, effects of pile-up and from the underlying event (UE) are corrected for on an event-by-event based estimation using

the ambient transverse energy density [43]. This density is determined as the median energy density of jets in the two regions of $|\eta| < 1.5$ and $1.5 < |\eta| < 3$ using the k_t-algorithm [44] with radius $R = 0.5$. The resulting isolation variable $E_{\mathrm{T}}^{\mathrm{iso},0.2}$ can be negative and photons with negative isolation values are kept. The background contribution decreases with the E_{T} of the photon, and therefore, an E_{T} dependent isolation requirement is better suited than a constant one. The requirement $E_{\mathrm{T},\gamma_{1(2)}}^{\mathrm{iso},0.2} < 0.05 \cdot E_{\mathrm{T},\gamma_{1(2)}}$ is used in the signal region. It is relaxed to $0.05 \cdot E_{\mathrm{T},\gamma_{1(2)}} < E_{\mathrm{T},\gamma_{1(2)}}^{\mathrm{iso},0.2} < 0.15 \cdot E_{\mathrm{T},\gamma_{1(2)}}$ for photon candidates in the control regions.

4.2 Event selection

The event selection is based on the properties of the leading (γ_1) and subleading (γ_2) photon candidates in each event. Requirements are applied on the transverse energy, the pseudorapidity, the isolation and the identification of the two photons as well as on their angular separation. The signal region is defined by the criteria summarised in Table 1. With these signal requirements approximately 4 709 000 events are selected in the data.

Table 1: Overview of the signal selection at the detector level and at the particle level.

Selection	Detector level	Particle level
Photon kinematics	$E_{\mathrm{T},\gamma_{1(2)}} > 40(30)$ GeV, $\quad |\eta_\gamma| < 2.37$ excluding $1.37 < |\eta_\gamma| < 1.52$	
Photon identification	tight	stable, not from hadron decay
Photon isolation	$E_{\mathrm{T},\gamma}^{\mathrm{iso},0.2} < 0.05 \cdot E_{\mathrm{T},\gamma}$	$E_{\mathrm{T},\gamma}^{\mathrm{iso},0.2} < 0.09 \cdot E_{\mathrm{T},\gamma}$
Diphoton topology	$N_\gamma \geq 2, \quad \Delta R_{\gamma\gamma} > 0.4$	

4.2.1 Details of the particle-level selection

The particle level selection, to which the data are unfolded to (cf. Sec. 6) closely follows the detector-level signal requirements, and is also shown in Table 1. Some aspects are clarified in detail in the remainder of this section.

The particle-level event selection in MC samples takes the leading two photons into account and vetoes the event if one of them is not prompt or fails the fiducial cuts.

The transverse isolation energy at particle level is determined as the sum of the transverse energies of all stable particles[3] excluding particles from pile-up, muons, neutrinos and the photon itself. Furthermore, to match the side effects of the UE subtraction at detector level also at the particle-level [4], a final-state based subtraction using the same method as described in Sec. 4.1 is applied. The value of the isolation requirement at the particle level (0.09) is chosen to be different from the one at the detector level (0.05). This difference accounts for the non-compensating nature of the ATLAS calorimeter, and the particle-level value has been optimised to minimise the number of events where photons pass a detector-level isolation requirement but fail the particle-level one, or vice versa.

[3] Stable particles are defined as those with a decay length $c\tau > 10$ mm.

[4] While there is no pile-up at particle level, there are still other effects, e.g. multiple parton interactions, that can cause such a subtraction procedure to have an influence.

4.3 Observables

Cross sections are measured differentially as functions of several observables defined for the diphoton system:

- Transverse energy E_{T,γ_1} (E_{T,γ_2}) of the leading (subleading) photon,
- Invariant mass $m_{\gamma\gamma}$ and transverse momentum $p_{\mathrm{T},\gamma\gamma}$ of the photon pair,
- Acoplanarity $\pi - |\Delta\phi_{\gamma\gamma}| = \pi - |\phi_{\gamma_1} - \phi_{\gamma_2}|$ of the photons,
- Transverse component of $p_{\mathrm{T},\gamma\gamma}$ with respect to the thrust axis:

$$a_{\mathrm{T},\gamma\gamma} = 2 \cdot \frac{|p_{x,\gamma_1} p_{y,\gamma_2} - p_{y,\gamma_1} p_{x,\gamma_2}|}{|\vec{p}_{\mathrm{T},\gamma_1} - \vec{p}_{\mathrm{T},\gamma_2}|},$$

  where $p_{x(y),\gamma_{1(2)}}$ are the $x(y)$-component of the leading (subleading) photon momenta, while $\vec{p}_{\mathrm{T},\gamma_1} - \vec{p}_{\mathrm{T},\gamma_2}$ is the transverse component of the momentum difference of both photons.

- The angular variable defined as:

$$\phi^*_\eta = \tan\frac{\pi - |\Delta\phi_{\gamma\gamma}|}{2} \sin\theta^*_\eta = \tan\frac{\pi - |\Delta\phi_{\gamma\gamma}|}{2} \sqrt{1 - \left(\tanh\frac{\Delta\eta_{\gamma\gamma}}{2}\right)^2},$$

  where $|\Delta\phi_{\gamma\gamma}|$ is the azimuthal distance between the two photons mapped into the range $[0, \pi]$, and $\Delta\eta_{\gamma\gamma} = \eta_{\gamma_1} - \eta_{\gamma_2}$. Angular variables are typically measured with better resolution than the photon energy. Therefore, a particular reference frame that allows ϕ^*_η to be expressed in terms of angular variables only, denoted by the subscript η and described in Ref. [45], is used in order to optimise the resolution. In particular, ϕ^*_η is ideal to probe QCD effects because it probes similar dynamics as $p_{\mathrm{T},\gamma\gamma}$, but with a significantly better resolution in the low-$p_{\mathrm{T},\gamma\gamma}$ region. A similar argument holds for $a_{\mathrm{T},\gamma\gamma}$.

- The scattering angle with respect to the beam axis in the Collins-Soper frame [46]:

$$|\cos\theta^*|^{(\mathrm{CS})} = \left|\frac{\sinh(\Delta\eta_{\gamma\gamma})}{\sqrt{1 + (p_{\mathrm{T},\gamma\gamma}/m_{\gamma\gamma})^2}} \cdot \frac{2E_{\mathrm{T},\gamma_1} E_{\mathrm{T},\gamma_2}}{m^2_{\gamma\gamma}}\right| = \left|\frac{p^+_{\gamma_1} p^-_{\gamma_2} - p^-_{\gamma_1} p^+_{\gamma_2}}{m_{\gamma\gamma} \cdot \sqrt{m^2_{\gamma\gamma} + p^2_{\mathrm{T},\gamma\gamma}}}\right|,$$

  with $p^\pm_\gamma = E_\gamma \pm p_{z,\gamma}$, where E_γ is the energy of the photon and $p_{z,\gamma}$ is the z-component of the momentum of the photon.

5 Background estimation

Reconstructed photon pairs can appear in the detector from a variety of sources beyond prompt production processes. These are summarised in this section along with details about how they are estimated and subtracted from the selected events to give the actual $\gamma\gamma$ signal yield. As a result, the purity of the diphoton ***signal*** is $(60.4^{+3.0}_{-2.8})\%$, where the uncertainties account for systematic and statistical sources as described in Sec. 7.

The ***jet background*** arises from jets mis-identified as photons and constitutes the main background. It consists of γj ($(19.9 \pm 1.2)\%$), $j\gamma$ ($(10.1^{+1.0}_{-0.9})\%$), or jj ($(6.3^{+1.2}_{-1.0})\%$) events with one or two jets mis-identified as photons, respectively. The data-driven determination is described in detail in Sec. 5.1. The notation $j\gamma$ (yj) here and in the following refers to the component where the leading (sub-leading) photon candidate stems from a mis-identified jet, while in jj events both photon candidates do.

Another $(2.6 \pm 0.1)\%$ of the sample corresponds to the ***electron background (ee)***, with the electrons[5] being mis-identified as or radiating photons. The main process contributing to this background is Drell-Yan production. It is estimated using the MC simulation described in Sec. 3.2 and is only visible in analysis regions with $m_{\gamma\gamma} \sim m_Z$.

Finally, $(0.6^{+0.5}_{-0.3})\%$ of the sample is associated to ***pile-up background (PU)***, i.e. pairs of γj events from different pp collisions on the same bunch crossing. It is determined with a data-driven approach discussed in Sec. 5.2.

The selected diphoton data sample can also contain signal events in which the two photon candidates come from the decay of a Higgs boson. Their contribution to the signal region is predicted to be 0.2% of the integrated signal and increases to a few percent in the relevant $m_{\gamma\gamma}$ bin. This contribution is not subtracted from the data as background, since it is a genuine part of prompt-photon pair production and thus considered to be signal.

5.1 Jet background

The background from jets mis-identified as prompt photons is estimated using a data-driven method, extrapolating the amount from multiple control regions enriched in background to the signal region. This is done performing a likelihood fit and is an extension to the two-photon case of the "two-dimensional sideband" technique used in the single photon analyses [7, 8, 10, 47–53]. It is similar to the method used in previous diphoton analyses [3, 4]. The fit is performed separately in each bin of each observable; in the description presented below, the labels that refer to the bins in each observable are not included.

To define the control regions, the selection on two almost independent jet-photon discriminant variables are reversed with respect to the signal selection: the photon f_{side} and w_{s3} shower-shape variables and the photon isolation, as defined in Sec. 4.1.

In addition to the signal region, where both photons pass both isolation and identification criteria, 15 background control regions are defined representing all possible combinations where at least one photon fails at least one of the criteria. These regions are labelled by index $i = 1 \ldots 16$, with $i = 1$ being the signal region. As an example, the isolation distributions for the sub-leading photon in MC signal events and those events in data that fail the identification criteria, and can be considered as background, are shown in Fig. 2.

To decompose the event sample, probability functions $f_{p,i}$ corresponding to the probability of an event from process $p \in \{\gamma\gamma, \gamma j, j\gamma, jj, ee, \text{PU}\}$ to fall in diphoton category i are defined. They are constructed as a product of the four probabilities for the each of the two photon candidates to fulfil both the isolation

[5] Electron here and in the following always refers to an electron or a positron.

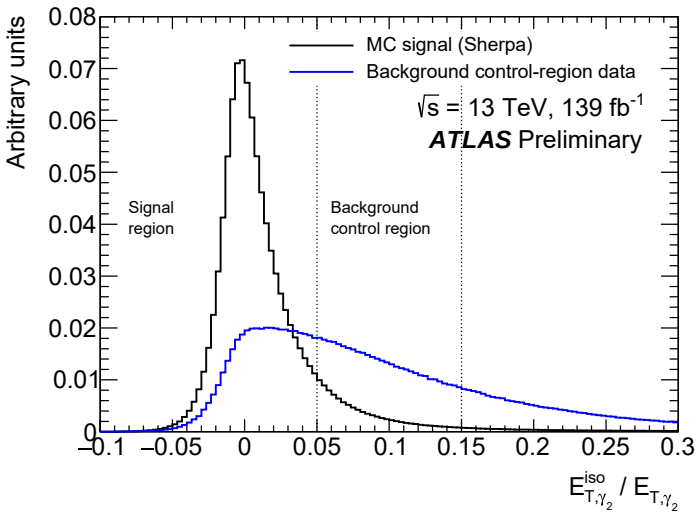

Figure 2: Relative photon isolation distribution for the subleading photon candidate as extracted from the SHERPA diphoton sample (black histogram) and from mis-identified jets extracted from data events in the non-tight control region (blue histogram).

and identification requirements of the category according to

$$f_{p,i} = f_{p,i}(\varepsilon^{\text{iso}}_{p,1},\ \varepsilon^{\text{iso}}_{p,2},\ R^{\text{iso}}_{p},\ \varepsilon^{\text{id}}_{p,1},\ \varepsilon^{\text{id}}_{p,2},\ R^{\text{id}}_{p},\ R^{\text{iso-id}}_{p,1},\ R^{\text{iso-id}}_{p,2})$$

$$= \begin{cases}
\varepsilon^{\text{iso}}_{p,1} & \varepsilon^{\text{iso}}_{p,2} & \varepsilon^{\text{id}}_{p,1} & \varepsilon^{\text{id}}_{p,2} & \text{for } i=1 \\
\varepsilon^{\text{iso}}_{p,1} & (1-\varepsilon^{\text{iso}}_{p,2}) & \varepsilon^{\text{id}}_{p,1} & \varepsilon^{\text{id}}_{p,2} & \text{for } i=2 \\
(1-\varepsilon^{\text{iso}}_{p,1}) & \varepsilon^{\text{iso}}_{p,2}R^{\text{iso}}_{p} & \varepsilon^{\text{id}}_{p,1} & \varepsilon^{\text{id}}_{p,2} & \text{for } i=3 \\
(1-\varepsilon^{\text{iso}}_{p,1}) & (1-\varepsilon^{\text{iso}}_{p,2}R^{\text{iso}}_{p}) & \varepsilon^{\text{id}}_{p,1} & \varepsilon^{\text{id}}_{p,2} & \text{for } i=4 \\
\varepsilon^{\text{iso}}_{p,1} & \varepsilon^{\text{iso}}_{p,2}R^{\text{iso-id}}_{p,2} & \varepsilon^{\text{id}}_{p,1} & (1-\varepsilon^{\text{id}}_{p,2}) & \text{for } i=5 \\
\varepsilon^{\text{iso}}_{p,1} & (1-\varepsilon^{\text{iso}}_{p,2}R^{\text{iso-id}}_{p,2}) & \varepsilon^{\text{id}}_{p,1} & (1-\varepsilon^{\text{id}}_{p,2}) & \text{for } i=6 \\
(1-\varepsilon^{\text{iso}}_{p,1}) & \varepsilon^{\text{iso}}_{p,2}R^{\text{iso}}_{p}R^{\text{iso-id}}_{p,2} & \varepsilon^{\text{id}}_{p,1} & (1-\varepsilon^{\text{id}}_{p,2}) & \text{for } i=7 \\
(1-\varepsilon^{\text{iso}}_{p,1}) & (1-\varepsilon^{\text{iso}}_{p,2}R^{\text{iso}}_{p}R^{\text{iso-id}}_{p,2}) & \varepsilon^{\text{id}}_{p,1} & (1-\varepsilon^{\text{id}}_{p,2}) & \text{for } i=8 \\
\varepsilon^{\text{iso}}_{p,1}R^{\text{iso-id}}_{p,1} & \varepsilon^{\text{iso}}_{p,2} & (1-\varepsilon^{\text{id}}_{p,1}) & \varepsilon^{\text{id}}_{p,2}R^{\text{id}}_{p} & \text{for } i=9 \\
\varepsilon^{\text{iso}}_{p,1}R^{\text{iso-id}}_{p,1} & (1-\varepsilon^{\text{iso}}_{p,2}) & (1-\varepsilon^{\text{id}}_{p,1}) & \varepsilon^{\text{id}}_{p,2}R^{\text{id}}_{p} & \text{for } i=10 \\
(1-\varepsilon^{\text{iso}}_{p,1}R^{\text{iso-id}}_{p,1}) & \varepsilon^{\text{iso}}_{p,2}R^{\text{iso}}_{p} & (1-\varepsilon^{\text{id}}_{p,1}) & \varepsilon^{\text{id}}_{p,2}R^{\text{id}}_{p} & \text{for } i=11 \\
(1-\varepsilon^{\text{iso}}_{p,1}R^{\text{iso-id}}_{p,1}) & (1-\varepsilon^{\text{iso}}_{p,2}R^{\text{iso}}_{p}) & (1-\varepsilon^{\text{id}}_{p,1}) & \varepsilon^{\text{id}}_{p,2}R^{\text{id}}_{p} & \text{for } i=12 \\
\varepsilon^{\text{iso}}_{p,1}R^{\text{iso-id}}_{p,1} & \varepsilon^{\text{iso}}_{p,2}R^{\text{iso-id}}_{p,2} & (1-\varepsilon^{\text{id}}_{p,1}) & (1-\varepsilon^{\text{id}}_{p,2}R^{\text{id}}_{p}) & \text{for } i=13 \\
\varepsilon^{\text{iso}}_{p,1}R^{\text{iso-id}}_{p,1} & (1-\varepsilon^{\text{iso}}_{p,2}R^{\text{iso-id}}_{p,2}) & (1-\varepsilon^{\text{id}}_{p,1}) & (1-\varepsilon^{\text{id}}_{p,2}R^{\text{id}}_{p}) & \text{for } i=14 \\
(1-\varepsilon^{\text{iso}}_{p,1}R^{\text{iso-id}}_{p,1}) & \varepsilon^{\text{iso}}_{p,2}R^{\text{iso}}_{p}R^{\text{iso-id}}_{p,2} & (1-\varepsilon^{\text{id}}_{p,1}) & (1-\varepsilon^{\text{id}}_{p,2}R^{\text{id}}_{p}) & \text{for } i=15 \\
(1-\varepsilon^{\text{iso}}_{p,1}R^{\text{iso-id}}_{p,1}) & (1-\varepsilon^{\text{iso}}_{p,2}R^{\text{iso}}_{p}R^{\text{iso-id}}_{p,2}) & (1-\varepsilon^{\text{id}}_{p,1}) & (1-\varepsilon^{\text{id}}_{p,2}R^{\text{id}}_{p}) & \text{for } i=16.
\end{cases} \quad (1)$$

Here, $\varepsilon^{\text{iso}}_{p,n}$ ($\varepsilon^{\text{id}}_{p,n}$) is the efficiency of the leading ($n = 1$) or subleading ($n = 2$) photon candidate, to fulfill the signal region isolation (identification) requirement with respect to the looser requirements that include the control regions. The correlation correction factors R account either for correlations between the isolation and identification of one photon candidate, $R^{\text{iso–id}}_{p,n}$, or for correlations between the isolation (identification) of both candidates, R^{iso}_{p} (R^{id}_{p}). $R = 1$ corresponds to no correlation between the relevant variables, while values below or above unity indicate a certain degree of positive or negative correlation, respectively.

The expected number of events n^{exp}_i in each region i can then be written as:

$$n^{\text{exp}}_i = \frac{n_{\gamma\gamma}}{\varepsilon^{\text{id}}_{\gamma\gamma,1}\,\varepsilon^{\text{iso}}_{\gamma\gamma,1}\,\varepsilon^{\text{id}}_{\gamma\gamma,2}\,\varepsilon^{\text{iso}}_{\gamma\gamma,2}}\, f_{\gamma\gamma,i} + N_{\gamma j} f_{\gamma j,i} + N_{j\gamma} f_{j\gamma,i} + N_{jj} f_{jj,i} + N_{ee} f_{ee,i} + N_{\text{PU}} f_{\text{PU},i}. \tag{2}$$

Here, $N_{\gamma\gamma}$, $N_{\gamma j}$, $N_{j\gamma}$, and N_{jj} are the total number of events attributed to the signal or background processes, respectively. The parameter of interest, i.e. the number of $\gamma\gamma$ events in the signal region, is given by $n_{\gamma\gamma} \equiv N_{\gamma\gamma} \cdot \varepsilon^{\text{id}}_{\gamma\gamma,1}\,\varepsilon^{\text{iso}}_{\gamma\gamma,1}\,\varepsilon^{\text{id}}_{\gamma\gamma,2}\,\varepsilon^{\text{iso}}_{\gamma\gamma,2}$. The total number of electron background events, N_{ee}, and of pile-up background events, N_{PU}, are fixed parameters in the fit. The other parameters are either pre-determined as described in Sec. 5.1.1 (thus reducing the number of parameters from Eq. (1) to Eq. (2)), or left as floating nuisance parameters in the likelihood fit. The likelihood function for a given observable bin is given by

$$\mathcal{L}(n_{\gamma\gamma},\, \theta |\, \vec{n}^{\text{obs}}) = \prod_i \frac{\left[n^{\text{exp}}_i(n_{\gamma\gamma},\, \theta)\right]^{n^{\text{obs}}_i}}{n^{\text{obs}}_i!} e^{-n^{\text{exp}}_i(n_{\gamma\gamma},\, \theta)}, \tag{3}$$

where θ is the set of 13 nuisance parameters floating in the fit in addition to $n_{\gamma\gamma}$:

$$\theta = \{N_{\gamma j},\, \varepsilon^{\text{id}}_{\gamma j,2},\, \varepsilon^{\text{iso}}_{\gamma j,2},\, N_{j\gamma},\, \varepsilon^{\text{id}}_{j\gamma,1},\, \varepsilon^{\text{iso}}_{j\gamma,1},\, N_{jj},\, \varepsilon^{\text{id}}_{jj,1},\, \varepsilon^{\text{iso}}_{jj,1},\, \varepsilon^{\text{id}}_{jj,2},\, \varepsilon^{\text{iso}}_{jj,2},\, R^{\text{id}}_{jj},\, R^{\text{iso}}_{jj}\}. \tag{4}$$

All nuisance parameters are associated with jets misidentified as photons, for which the reconstruction efficiencies and correlations are not known accurately, thus motivating this sophisticated approach.

The result of the fit for the inclusive data sample can be seen for each of the 16 regions in Fig. 3. As mentioned above, results are also obtained in each observable bin separately, and the equivalent decomposition in the signal region is displayed differentially in Fig. 4. The purity of the $\gamma\gamma$ signal process ranges from 35% at low invariant mass up to 80% at high E_{T}.

5.1.1 Fit model input parameters

The fit model introduced in the previous section relies on several pre-determined parameters, which are described below. In order to take into account the systematic uncertainties on these input parameters, the fit is repeated with systematic variations of the corresponding parameter values.

Signal parameters: $\varepsilon^{\text{id}}_{\gamma\gamma,1}$, $\varepsilon^{\text{id}}_{\gamma\gamma,2}$, $R^{\text{id}}_{\gamma\gamma}$, $\varepsilon^{\text{iso}}_{\gamma\gamma,1}$, $\varepsilon^{\text{iso}}_{\gamma\gamma,2}$, $R^{\text{iso}}_{\gamma\gamma}$, $R^{\text{iso–id}}_{\gamma\gamma,1}$ and $R^{\text{iso–id}}_{\gamma\gamma,2}$

The values of the eight $\gamma\gamma$ signal parameters are extracted from the MC simulation based on the Sherpa signal sample, corrected to match the isolation and identification variable distributions in data [41, 54]. These parameters are extracted as a function of each observable for which the differential cross section is measured. Uncertainties on these parameters due to the detector simulation and theory modelling, in particular for the isolation distribution, are taken into account as described in Sec. 7.2 and 7.3.

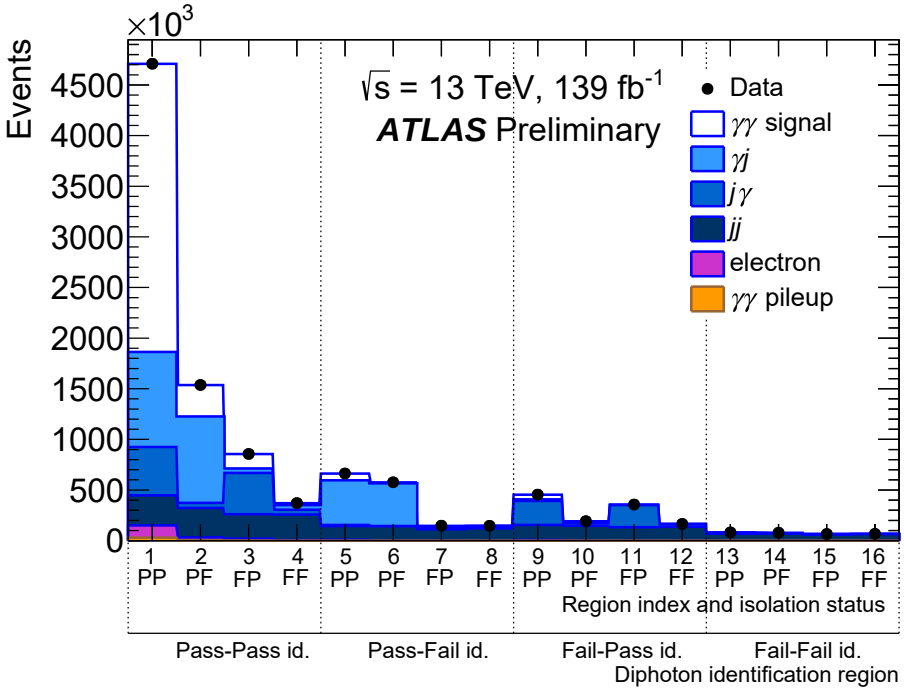

Figure 3: Event yields of the inclusive data sample in the 16 diphoton regions. Both the observed counts and the post-fit predictions of the signal and each background component are shown. Labels "PP/PF/FP/FF" are used to denote the isolation status ("P"=pass, "F"=fail) of the leading and subleading photon candidates.

Correlation between isolation and identification: $R^{\text{iso-id}}_{\gamma j,2}$ and $R^{\text{iso-id}}_{j\gamma,1}$

The correlation between isolation and identification for jets mis-identified as photons is parametrised by the $R^{\text{iso-id}}_{j} \equiv R^{\text{iso-id}}_{\gamma j,2} = R^{\text{iso-id}}_{j\gamma,1}$ correction factor. A twofold approach is used to estimate it. First, a γj MC sample is used to estimate this parameter from simulation, yielding $R^{\text{iso-id,MC}}_{j} = 0.99 \pm 0.03$ (stat) without a significant trend as a function of E_{T} within the limited MC statistics. In addition to the MC study, a γj-rich validation region in data is constructed by requiring the subleading photon to fail an isolation requirement based on the sum of the transverse momenta of charged-particle tracks coming from the primary vertex, and subtracting the contamination of $\gamma\gamma$ events in that region using the signal MC simulation. With a higher statistical power in data, an increase in correlation as a function of E_{T} is observed. This dependency is extrapolated to the signal region using the MC simulation. For the final results, an average of the MC and data results is used differentially, with central values varying in a range of $0.93 < R^{\text{iso-id}}_{j} < 1$ with E_{T}, and with uncertainties propagated, as described in Sec. 7.1.

Correlation between isolation in γj and $j\gamma$ events: $R^{\text{iso}}_{\gamma j}$ and $R^{\text{iso}}_{j\gamma}$

The correction factor R^{iso}_{p} parametrises the correlation between the isolation variables of the two photon candidates. For the signal pdf, this parameter is extracted from MC as $R^{\text{iso}}_{\gamma\gamma}$. A similar extraction for fake photons from γj MC samples alone is not possible because of the limited statistical precision available. A slight correlation is expected, as found for the signal pdf, where $0.95 < R^{\text{iso}}_{\gamma\gamma} < 1$. It can also be extracted in jj background events, where R^{iso}_{jj} is left to float in the fit and yields values in the range $0.9 < R^{\text{iso}}_{jj} < 1$. For the γj and $j\gamma$ backgrounds, $R^{\text{iso}}_{\gamma j} = R^{\text{iso}}_{j\gamma} = 0.95 \pm 0.05$ is chosen in

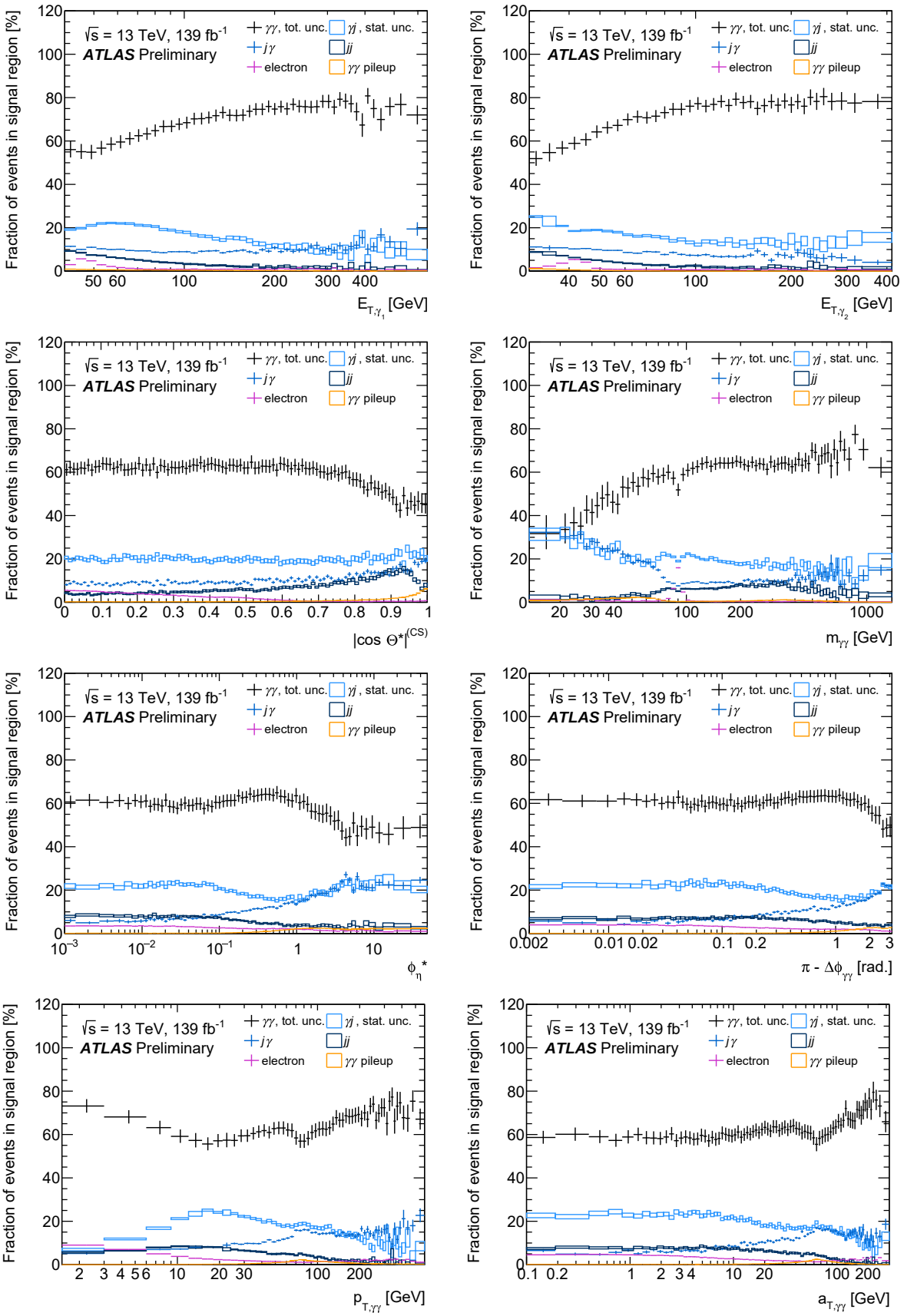

Figure 4: Sample decomposition as a function of each observable. For the $\gamma\gamma$ signal fraction, the total uncertainty is shown, while for the background fractions only the data and Monte Carlo statistical uncertainty component is shown.

all regions of phase space, thus the uncertainties cover the extreme cases.

Photon isolation and identification efficiencies in γj: $\varepsilon^{\text{iso}}_{\gamma j,1}$, $\varepsilon^{\text{iso}}_{j\gamma,2}$, $\varepsilon^{\text{id}}_{\gamma j,1}$, $\varepsilon^{\text{id}}_{j\gamma,2}$
For the γj and $j\gamma$ background components, isolation and identification efficiencies for the prompt photons are derived from the $\gamma\gamma$ signal MC sample. The underlying assumption is cross-checked by comparing these efficiencies to the ones derived in the γj SHERPA MC sample. The efficiencies are compatible within statistical uncertainties.

Identification correlation in γj events: $R^{\text{id}}_{\gamma j}$ and $R^{\text{id}}_{j\gamma}$
The correlation between the identification of the two objects is in general very low. This is cross-checked with MC simulation for the $\gamma\gamma$ signal process. Performing the fit with extreme values of $R^{\text{id}}_{\gamma j}$ and $R^{\text{id}}_{j\gamma}$ determined from MC simulation results in negligible variations of the final result. The assumption $R^{\text{id}}_{\gamma j} = R^{\text{id}}_{j\gamma} = 1$ is thus kept without an additional uncertainty.

5.2 Pile-up of multiple single-photon events

Pairs of γj events from different pp collisions in the same bunch crossing can form a diphoton final state in the detector. The normalisation of this background is estimated using a fit to the data. The shape of the background in the diphoton observables is based on MC simulations. Details of the procedure are given below.

The background is estimated selecting diphoton candidate events in data in which both photons converted to electron-positron pairs within the detector material and both are required to have $|\eta| < 1.45$[6]. The resulting tracks are required to be reconstructed in the inner tracking detector and the conversion point is required to be measured within the volume of the silicon pixel or strip detector. These tracks thus provide precise information about the longitudinal position z_γ of the vertex along the beam in which the photon is produced, thus providing means to differentiate whether the two photons come from the same primary vertex. This information is used in a two-component template fit to $\Delta z = |z_{\gamma_1} - z_{\gamma_2}|$, as can be seen in Fig. 5.

The first component of the template, representing the distribution of pile-up events in Δz, is considered to be a convolution of the two individual longitudinal Gaussian z_{PV} distributions which have a width of $\sigma_z = 35$ mm, resulting in a Gaussian with a width of $\sigma_{\Delta z} = \sqrt{2} \times \sigma_z$. The second component of the template, representing the non-pile-up contribution, is taken as a power-law function. To extract the fraction of the pile-up events, the power-law parameters and the normalisation of each component are fitted simultaneously to the measured Δz distribution. The fit is performed in two regions simultaneously, $\Delta\phi_{\gamma\gamma} < \pi/2$ and $\Delta\phi_{\gamma\gamma} > \pi/2$, where the pile-up background fraction in the first region is about a factor 10 higher than in the second. The fit yields an uncertainty of $\delta^{\text{PU}}_{\text{fit}} = \pm 15\%$ on the pile-up background fraction.

The event yield resulting from this fit still contains contributions from fake photons, which are subtracted in the main background fit also for pile-up events. To avoid a double subtraction, the nominal background fit is performed for the events with $\Delta z > 48$ mm to determine the fraction of prompt $\gamma\gamma$ events within the pile-up contribution. The large uncertainty of $\delta^{\text{PU}}_{\text{signal}} = \pm 50\%$ on this fraction is of statistical nature due to the low number of input events, and is added in quadrature with the $\delta^{\text{PU}}_{\text{fit}}$ to form the total uncertainty on the pile-up background propagated to the final results, as described in Sec. 7.

[6] The fraction of converted photons is fairly constant as a function of photon E_{T} and η and well modelled in MC. The conversion events can thus be used directly for an extrapolation to the full dataset.

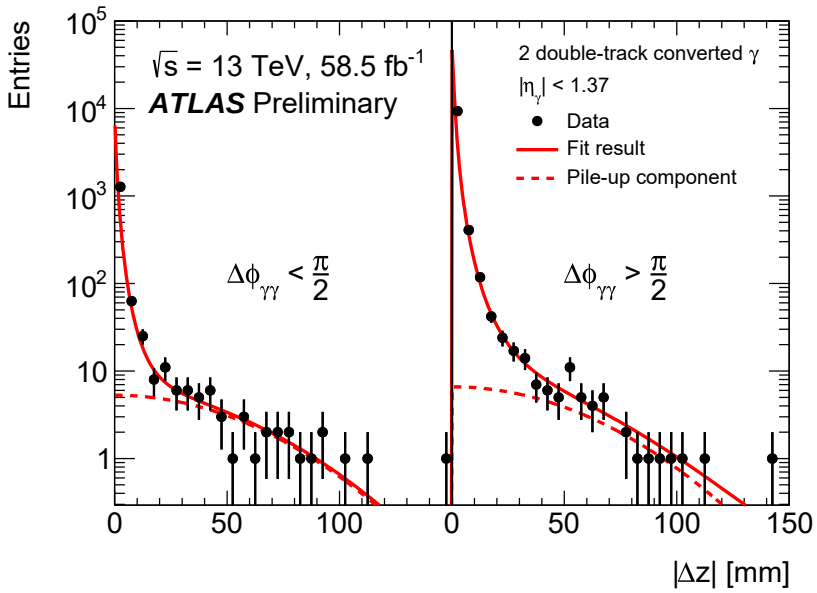

Figure 5: The two-component template fit to determine the global normalisation of pile-up events is shown. Data events in which each of the two photon candidates is associated with two inner detector tracks are used for the fit. The dashed lines represent the pile-up-like component of the total template marked with a solid line.

With the normalisation of the pile-up background fixed, the shape of this background in the fiducial phase space and as a function of each observable is derived using a sample of pseudo-events. Events in this sample are constructed by overlaying two separate reconstructed events from a γj MC simulation. This shape is combined with the normalisation determined as above and fed into the background estimation fit as a pre-determined component.

6 Correction to particle level

Detector effects due to finite resolution and inefficient detection of particles have to be corrected for in order to be able to compare results from different experiments and to allow comparisons to theory without detector simulation. The unfolding procedure is applied to the background subtracted distribution at the detector level in three steps.

First the measured distribution is corrected for the fraction of reconstructed MC events that do not pass the particle-level selection. The contribution of these unmatched reconstructed events is estimated using the signal MC samples. The main source of unmatched photons are due to the transverse energy and the photon isolation requirements. The particle-level selection is chosen close to the detector-level selection to reduce the influence of this correction.

The second step is to correct for detector resolution effects which cause migrations from one particle-level bin to multiple detector-level bins. For this step, an iterative unfolding method [55] based on Bayes' theorem is used. Response matrices parametrise these migrations and are constructed from simulated events passing both the detector-level and particle-level selections. A first iteration of the migration correction uses the particle-level prediction as the prior input. The prior then gets updated with each of the three iterations

Table 2: Breakdown of the relative uncertainties on the integrated fiducial cross section measurement.

Source	Relative uncertainty [%]
Background estimation	4.3
$R_j^{\text{iso}-\text{id}}$	4.2
$\gamma\gamma$ pile-up background	0.6
$R_{\gamma\text{j}}^{\text{iso}}$	0.5
Electron background	0.2
Photon isolation	4.0
Pile-up reweighting	3.5
Photon isolation	1.9
Photon identification	3.0
Other	4.1
Data-period stability	3.6
Luminosity	1.7
Trigger efficiency	0.7
MC Sherpa/Pythia	0.6
Signal modelling of E_{T,γ_1}	0.2
MC statistical uncertainty	0.1
Unfolding method	<0.1
Photon energy	0.5
Total systematic uncertainty	7.8
Data statistical uncertainty	0.3

used in this analysis; the number was chosen high enough to minimise the dependence on the prior but low enough to not be sensitive to large statistical uncertainties.

In the last step, the unfolded results are corrected for detector inefficiencies. This accounts for the fraction of particle-level events in the signal region which do not pass the signal selections at detector-level. Their contribution is also estimated using the signal MC samples. The largest corrections stem from the photon identification and isolation selection. The efficiency and unmatched-photon corrections partially cancel each other due to the symmetric shape of the detector response, e.g. for the photon transverse energy criteria.

7 Uncertainties

Several uncertainties affect the measurement. They are evaluated independently and then added in quadrature as uncorrelated components into a total uncertainty, with its breakdown shown in Table 2 for the integrated fiducial cross section. Fig. 6 shows the breakdown of the systematic uncertainties in the differential cross section.

The individual sources of uncertainties and the methods to propagate them to the final result are described in more detail in the following section.

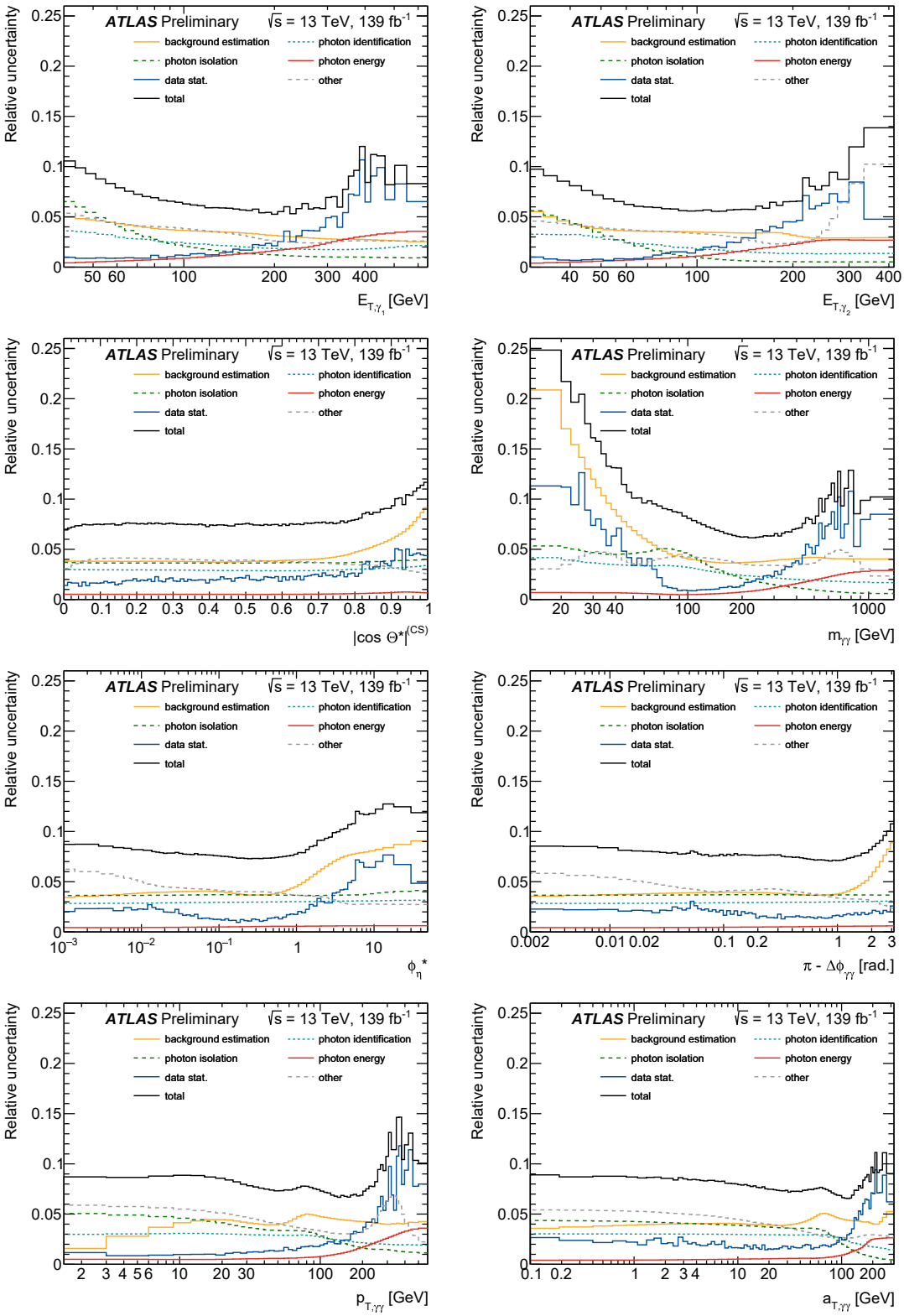

Figure 6: The relative uncertainties on the unfolded result associated to different sources are summarised. The uncertainty components and the total uncertainty are shown as a function of each of the observables.

7.1 Background estimation

Fake photons from jets. Among the input parameters to the background fit described in Sec. 5, the variation of only two of the parameters yields a non-negligible impact on the final result. The correlation between isolation and identification of fake photons from jets, $R_j^{\text{iso}-\text{id}}$, is determined both from MC simulations as well as in a data-driven approach, as described above. While the average between both methods is used for the central value, half of the difference is assigned as an uncertainty to cover both approaches, and additionally combined in quadrature with the statistical uncertainty on the MC result. This is by far the dominant contribution to the total uncertainty for the background, which amounts to 3.5% in general and rises up to 17% in the low-$m_{\gamma\gamma}$ region. The correlation between the photon and jet isolation in γj and $j\gamma$ events is varied around its central value by ±5%, as determined from cross checks in a γj MC sample and in the control regions dominated by jj events in data. This uncertainty is at the sub-percent level almost everywhere, except at low $m_{\gamma\gamma}$, where it rises up to 6%.

Fake photons from electrons. Three components are taken into account as uncertainties for the electron-related background sources. The physics modelling of the $Z \to ee$ MC sample is varied by a 5% uncertainty on the normalisation, and a p_{T}^{Z}-dependent shape uncertainty covering the difference between MC and data [35]. The uncertainty related to the modeling of $e \to \gamma$ fake rates is estimated from a dedicated measurement using $Z \to ee$ events. All of these uncertainties have a completely negligible contribution almost everywhere, rising to 2% only in the $m_{\gamma\gamma} \sim m_Z$ bin.

Pile-up background. The uncertainty on the normalisation of the pile-up background stems from a combination of two uncertainties arising from the fits, namely the fit to extract the total pile-up yield, and the $\gamma\gamma$ signal extraction in the pile-up sample. The main impact of this background contribution is located at $|\cos\theta^*|^{(\text{CS})} \to 1$ (see Fig. 4) and its uncertainty rises to 6% in this region, whereas it is small in all other regions of phase space.

The uncertainties described above are propagated to the final cross section results by using different background-subtracted signal yields as input to the unfolding procedure, with all bins varied in a correlated way, and response matrices unaffected.

7.2 Photon selection

The detector simulation and reconstruction of photons within the MC samples play significant roles in the background estimation and unfolding. This results in uncertainties from various sources.

Photon isolation. The modelling of the photon isolation variable in simulated events is corrected using a data-driven technique when deriving the nominal results [41]. An uncertainty due to a potential isolation mismodelling is estimated by disabling these data-driven corrections. This affects mainly the position of the peak of the isolation variable. Additionally, the width of the isolation transverse energy distribution is affected significantly by the modelling of pile-up in the simulation. To estimate this uncertainty, results are also obtained with reduced and increased amounts of pile-up in the simulation. The latter dominates the isolation uncertainty and constitutes the second leading source of uncertainty in the analysis, with a typical size of 4%.

Photon trigger and identification efficiency. The uncertainties on the modelling of the detector efficiency of the photon trigger and identification are addressed using scale factors. The scale factors are derived to match the detector efficiency in simulation to data [54] and are affected by systematic uncertainties. They are applied as an event weight depending on the transverse energy E_{T} and pseudo-rapidity η of the photon. While the trigger efficiency uncertainty is negligible everywhere, the photon identification efficiency uncertainty ranges between 2% and 4%.

Photon energy. Uncertainties of the detector modelling of the photon energy scale and resolution are taken into account by modifying the MC simulation used to determine response matrices, efficiencies and unmatched-photon rates [38]. This is done separately for independent sources of the uncertainty, e.g. from the overall energy scale determined in $Z \to ee$ decays; the non-linearity of the energy measurement at the calorimeter cell level; the relative calibration of the different calorimeter layers; the amount of material in front of the calorimeter; and the modelling of the photon conversion reconstruction, lateral shower shape, and energy resolution. They are propagated separately to account for correlations and their η dependence and are combined in quadrature. This uncertainty is at the sub-percent level in most regions of the analysis, rising to 3% only at high transverse energy and $m_{\gamma\gamma}$.

For the photon isolation and identification variations described above, modified MC simulations are used coherently in the background fit and unfolding, to propagate the uncertainty for each source to the final result and maintain the correlations. The photon energy and photon trigger efficiency uncertainty affect only the unfolding.

7.3 Other uncertainties

Signal theory modelling. The theory modelling in the signal MC can affect the correction to the particle level as well as the signal model parameters in the background fit. The resulting uncertainty is estimated by reweighting the nominal Sherpa sample in two different ways and repeating the whole analysis chain. The first reweighting is based on the photon isolation distribution taken from a Pythia8 sample at particle level. This procedure captures the dominant difference between both models without introducing significant statistical fluctuations. The uncertainty in the final results is relatively constant at the 1% level and rises up to 4% in the low-$m_{\gamma\gamma}$ region. Additionally, a reweighting of the leading photon transverse energy distribution such that the detector-level distribution matches the background-subtracted result is performed. The effect of this variation is below 1%. The differences between the nominal and each of the two reweighted results are treated as independent uncertainties and applied coherently in the background fit and the unfolding.

Unfolding method uncertainties. The results of the unfolding procedure can depend on the choice of prior and the number of iterations. To estimate an uncertainty, the MC simulation is reweighted such that it matches the data at the detector level, and this emulated data is then unfolded using the nominal sample. The non-closure with respect to the reweighted particle-level simulation then yields an additional uncertainty orthogonal to the one from signal theory modelling and is negligible everywhere.

Data period stability The compatibility of the results obtained by splitting the data and MC into 2015+2016, 2017 and 2018 periods is tested. The whole analysis is redone for these three individual datasets. An additional uncertainty is assigned to cover the non-closure among the different years. It is typically around 4%.

	fixed order accuracy						fragmentation		QCD	NP
	$\gamma\gamma$	$+1j$	$+2j$	$+3j$	$+\geq 4j$	$gg \to \gamma\gamma$	γj	jj	res.	eff.
DIPHOX	NLO	LO	-	-	-	LO	NLO		–	–
NNLOJET	NNLO	NLO	LO	-	-	LO	–	–	–	–
SHERPA	NLO		LO		PS	LO	ME+PS		PS	✓

Table 3: Overview of the theory predictions and their relevant features.

MC statistics. The influence of the limited size of the MC samples on the final result is evaluated using a bootstrap method. This is done coherently for the background fit and the unfolding. The resulting uncertainty is negligible everywhere.

Data statistics. The statistical uncertainty of the data sample is propagated from the signal extraction to the particle level using pseudo experiments. It is the dominant uncertainty at high E_{T} and high $m_{\gamma\gamma}$, but subleading in general.

Luminosity. The uncertainty in the combined 2015–2018 integrated luminosity is 1.7% [56], obtained using the LUCID-2 detector [57] for the primary luminosity measurements. This uncertainty is subleading in comparison to the other uncertainties.

8 Fixed-order predictions

In addition to the particle-level predictions from the fully-simulated SHERPA signal sample described in Sec. 3.2, the unfolded data are compared to further state-of-the-art theory predictions at fixed order, described below. All predictions are summarised in Table 3.

Fixed-order NNLO with NNLOJET. The NNLOJET framework [58] is used to obtain fixed-order predictions for diphoton production up to NNLO QCD accuracy. It is based on the antenna subtraction method [59, 60] and the NNLO prediction includes the loop-induced $gg \to \gamma\gamma$ contribution. The nominal factorisation and renormalisation scales are chosen as $\mu_{F,R} = m_{\gamma\gamma}$ and varied independently to estimate the perturbative uncertainties in a 7-point variation to $\mu_F = c_F \cdot m_{\gamma\gamma}$, $\mu_R = c_R \cdot m_{\gamma\gamma}$, where $c_{F,R} = 0.5, 1.0, 2.0$ with $0.5 \leq c_F/c_R \leq 2$. For the nominal predictions, the NNPDF 3.0 NNLO PDF set [25] is used. Comparisons of the nominal predictions and those based on the CT14 [61] and MMHT2014 [62] PDF sets are performed. Variations of the strong coupling parametrisation are also taken into account by switching to NNPDF 3.0 NNLO PDF sets with $\alpha_S(m_Z) = 0.117$ or 0.119. NNLO predictions for the fragmentation component are not yet available. Thus, the prediction is calculated only from the direct component using an implementation of the hybrid scheme for photon isolation [26, 63, 64]:

- a very loose smooth cone isolation [27] with $n = 2$, $\delta = 0.1$, $\varepsilon = 0.1$, and
- the experimental cone isolation with the fiducial photon isolation given in Table 1 but without the UE subtraction.

The smooth-cone isolation requirement is necessary to remove collinear photon-quark configurations from the calculation, which would be singular and would have to be factorised into a fragmentation function for a full calculation. The hybrid scheme helps to minimise the bias from not taking such configurations into account.

Fixed-order NLO with DIPHOX. Fixed-order NLO predictions including the direct, single- and double fragmentation contributions are made with DIPHOX [65] using CT10 NLO PDFs [66]. The nominal factorisation, renormalisation, and fragmentation scales are chosen as $\mu_R = \mu_F = \mu_{\text{frag}} = m_{\gamma\gamma}$. The loop-induced $gg \to \gamma\gamma$ process is included in the direct component at leading order. Since the fragmentation contributions are included, the DIPHOX predictions are valid for a cone-based photon isolation consistent with the one used in the measurement, $E_{\text{T},\gamma_{1(2)}}^{\text{iso},0.2} < 0.09 \cdot E_{\text{T},\gamma_{1(2)}}$. To estimate the perturbative uncertainties of the DIPHOX predictions, three sets of input parameters are varied. Factorisation and renormalisation scales undergo 7-point variations as defined above. This is the dominant uncertainty for this prediction. The fragmentation scale is varied by a factor of 2 up and down, yielding an uncertainty which is always significantly smaller than the factorisation and renormalisation scale variations. Finally, variations between predictions based on the nominal PDF set and those based on MSTW2008 [67] and NNPDF2.3 [28] are also significantly smaller than the scale variation in all phase-space regions.

The fixed-order predictions do not include non-perturbative effects. The impact of the non-perturbative effects is found to be negligible, except in soft or collinear regions of the phase space, where they grow to $O(10\%)$; in such regions, fixed-order predictions are not valid without resummation. Thus, no correction is applied to the fixed-order predictions.

9 Results

9.1 Integrated cross section in the fiducial phase space

The measurement of the differential cross section as a function of E_{T,γ_2} is used to compute the integrated fiducial cross section,

$$\sigma_{\gamma\gamma} = (30.9 \pm 0.1\ (\text{stat.}) \pm 2.4\ (\text{syst.}))\ \text{pb}.$$

The integration is also performed over the other differential cross section measurements yielding compatible results.

The comparison of the measured cross section with the theoretical predictions (see Fig. 7 and Table 4) shows the importance of higher-order QCD contributions even for such an inclusive diphoton measurement. The predictions from SHERPA MEPS@NLO, which has NLO multi-leg matrix elements supplemented by a parton shower, and that from the fixed-order NNLO prediction as implemented in NNLOJET are the only predictions compatible with the data within the uncertainties. The predictions limited to LO or NLO QCD, as implemented in NNLOJET (N)LO and DIPHOX NLO, fail to agree with the data within their estimated uncertainties.

9.2 Differential cross sections

The measured differential cross sections as functions of the different observables are shown in Figures 8 and 9. Comparisons between the data and DIPHOX NLO, NNLOJET NNLO and SHERPA MEPS@NLO predictions are also included for all observables. NNLOJET and SHERPA provide the best agreement with the data in the regions expected to be modelled well by perturbative QCD. Since DIPHOX and NNLOJET are fixed-order predictions, they are not expected to be valid in regions where the effects of multiple collinear or soft QCD emissions are relevant, while SHERPA provides a remarkably good agreement with the data also in these regions.

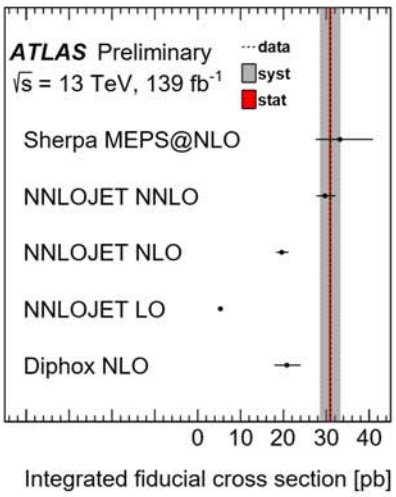

Figure 7: Integrated fiducial cross section comparison between ATLAS data and theory predictions.

Integ. fid. cross section [pb]	$\sigma_{\gamma\gamma}$	± syst	±stat
SHERPA MEPS@NLO	33.2	$^{+7.7}_{-5.6}$	<0.1
NNLOJET NNLO	29.7	$^{+2.4}_{-2.0}$	< 0.1
NLO	19.6	$^{+1.6}_{-1.3}$	< 0.1
LO	5.0	$^{+0.5}_{-0.5}$	< 0.1
DIPHOX NLO	20.8	$^{+3.2}_{-2.9}$	< 0.1
Data	30.9	2.4	0.1

Table 4: Integrated fiducial cross section from ATLAS data compared to theory predictions with their systematic uncertainties from QCD scale variations.

For the transverse energy spectrum of the leading photon, E_{T,γ_1}, NNLOJET and SHERPA predictions are compatible with the data over the full measured range. DIPHOX describes adequately the shape of the measured differential cross section, however, as already seen for the integrated cross section, the normalisation of this prediction is much lower than that of the data. A similar picture holds for the subleading photon, E_{T,γ_2}, with the only notable difference being the shape of the DIPHOX prediction, which describes adequately the shape of the measured cross section for $E_{\mathrm{T},\gamma_2} \geq 40$ GeV, but underestimates considerably the rate of photons at lower E_{T,γ_2} values.

Stark features of the theory predictions can be seen in the $m_{\gamma\gamma}$ spectrum. The shape of this distribution is governed by the transverse-energy requirements on the individual photons, with the region $m_{\gamma\gamma} < E_{\mathrm{T},\gamma_1} + E_{\mathrm{T},\gamma_2}$ being suppressed and only populated through $\gamma\gamma$+multi-jet configurations. Such configurations are not modelled well at NLO accuracy in DIPHOX, but benefit significantly from the higher-order contributions included in the NNLOJET and SHERPA predictions. The predictions from NNLOJET and SHERPA agree with the data within uncertainties, while the uncertainties in the DIPHOX prediction are severely underestimated judging from the higher-order predictions. At high $m_{\gamma\gamma}$, the SHERPA predictions are compatible with the data, while NNLOJET underestimates the rate slightly.

For high $p_{\mathrm{T},\gamma\gamma}$ Sherpa and Nnlojet agree well with the data, while for intermediate values the Nnlojet prediction is slightly too low to cover the data within uncertainties, and Sherpa is slightly high but still compatible. As expected, the fixed-order predictions fail at low $p_{\mathrm{T},\gamma\gamma} < 10\,\mathrm{GeV}$, where soft QCD emissions are relevant, while Sherpa provides a good agreement with the data also in this region of phase space.

The three observables $\pi - \left|\Delta\phi_{\gamma\gamma}\right|$, $a_{\mathrm{T},\gamma\gamma}$, and ϕ^*_η are closely related and reveal very similar features in the comparison between the data and theory predictions. The almost back-to-back configuration of the two photons ($\pi - \left|\Delta\phi_{\gamma\gamma}\right| < 0.1$, $a_{\mathrm{T},\gamma\gamma} < 10\,\mathrm{GeV}$, or $\phi^*_\eta < 0.1$), is difficult to model correctly with fixed-order predictions, because even almost collinear or low-energy parton emissions can decorrelate the two photons. Only the parton-shower based Sherpa prediction includes a resummation of these effects and is able to model the back-to-back region reliably, agreeing well with the data over the full measured range in these three observables. In the region of intermediate azimuthal separation of the photons ($\pi - \left|\Delta\phi_{\gamma\gamma}\right| \approx 1$, $a_{\mathrm{T},\gamma\gamma} \approx 40\,\mathrm{GeV}$, or $\phi^*_\eta \approx 0.5$) Nnlojet underestimates the data, while for a large decorrelation they agree well, in contrast to the NLO predictions from Diphox, which fail to accurately model the shape of these distributions over the full measured range.

For scattering angles close to the limit, $|\cos\theta^*|^{(\mathrm{CS})} \to 1$, the fixed-order predictions underestimate the measured rate. This region is sensitive to uncorrelated photons, which can occur as a consequence of the associated production of multiple jets. The NNLO prediction is affected by larger perturbative uncertainties in this region; this is an indication of the (N)LO-accurate associated production of two jets (one jet) becoming relevant. The multi-leg merged prediction from Sherpa provides a better description of the measured cross section in this region.

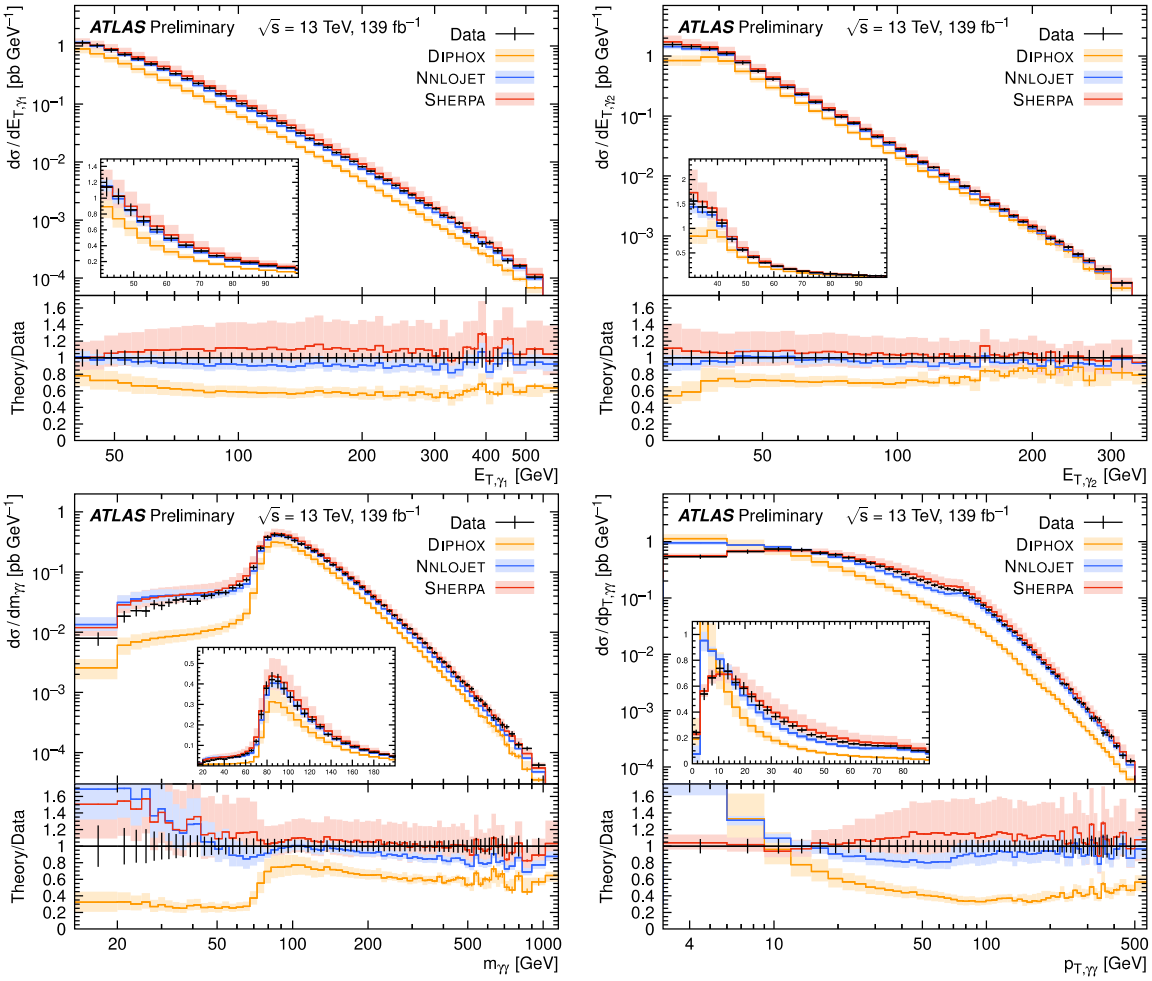

Figure 8: Differential cross sections as functions of E_{T,γ_1}, E_{T,γ_2}, $m_{\gamma\gamma}$ and $p_{\mathrm{T},\gamma\gamma}$ compared to the predictions from DIPHOX NLO, NNLOJET NNLO and SHERPA MEPS@NLO predictions. At the bottom of each plot, the ratio of the prediction to the data is shown. Uncertainty bars on the data represent the total uncertainty, while uncertainty bands (bars) on the predictions represent perturbative scale (statistical) uncertainties.

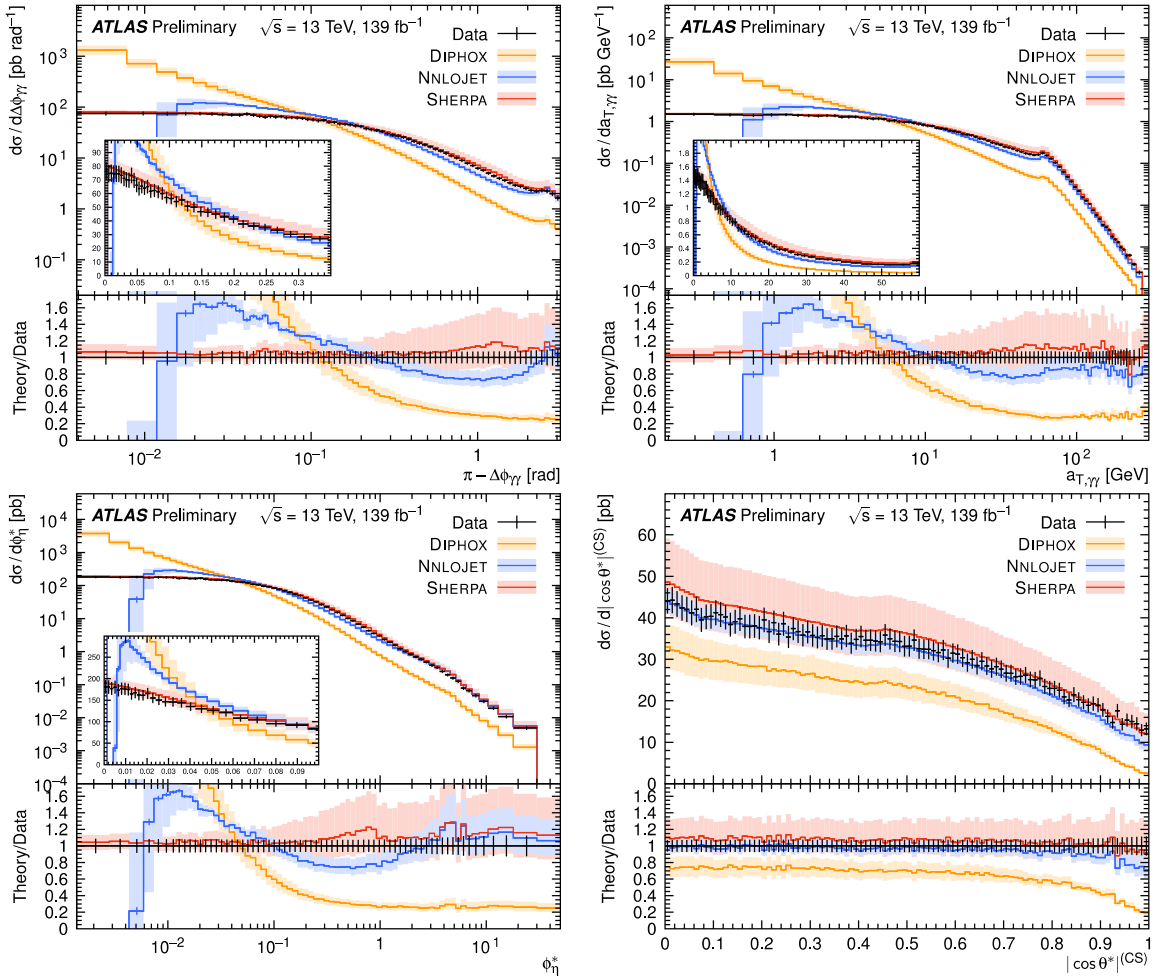

Figure 9: Differential cross sections as functions of $\pi - |\Delta\phi_{\gamma\gamma}|$, $a_{\mathrm{T},\gamma\gamma}$, ϕ^*_η and $|\cos\theta^*|^{(\mathrm{CS})}$ compared to the predictions from DIPHOX NLO, NNLOJET NNLO and SHERPA MEPS@NLO predictions. At the bottom of each plot, the ratio of the prediction to the data is shown. Uncertainty bars on the data represent the total uncertainty, while uncertainty bands (bars) on the predictions represent perturbative scale (statistical) uncertainties.

10 Conclusion

A measurement of prompt photon pair production in proton-proton collisions at $\sqrt{s} = 13$ TeV is presented. The data were recorded by the ATLAS detector at the LHC with an integrated luminosity of 139 fb^{-1}.

Events with two photons in the well-instrumented region of the detector are selected, and the photons are required to be isolated and have $E_{\mathrm{T},\gamma_{1(2)}} > 40$ (30) GeV for the leading (sub-leading) photon ordered in transverse energy. The dominant background stems from non-prompt photons from hadron decays, which is very challenging to estimate using simulation. A sophisticated data-driven method is used to estimate this background using background-rich control regions based on reverted photon identification and isolation requirements. Using a novel data-driven technique, also the small background from two photons being produced in separate proton-proton collisions in the same bunch crossing is taken into account, which will become even more relevant for future LHC runs.

The background-subtracted signal yields are corrected for detector efficiencies and migrations and converted into fiducial cross sections. The measured integrated fiducial cross section is (30.9 ± 2.4) pb. Differential cross sections as functions of several observables of the diphoton system are presented, including the transverse momenta of the leading (subleading) photon up to 550 (330) GeV, the invariant mass of the diphoton system from 15 GeV to 1 TeV, and the transverse momentum of the diphoton system up to 500 GeV. Specifically, diphoton variables sensitive to different aspects of higher-order corrections in perturbative QCD are studied and compared to theory predictions from state-of-the-art MC and fixed-order calculations.

Good agreement is generally found with the predictions at the highest theoretical precision. An impressive improvement is observed when taking into account higher-order terms in perturbative QCD. Only the merged approach with multi-leg matrix elements at NLO, as implemented by Sherpa, and a fixed-order NNLO calculation, as implemented by Nnlojet, give a satisfactory description of the data. The fixed-order NNLO calculation has a higher formal precision than Sherpa and thus lower theoretical uncertainties in the regions governed by perturbative QCD. The multi-leg merged prediction yields larger uncertainties, but is in better agreement with the data in all regions. Sherpa includes QCD resummation through the parton shower, and thus provides a more reliable prediction in regions sensitive to collinear or low-energy parton emissions. The shape of the measured cross section as a function of $m_{\gamma\gamma}$ is best described by the Sherpa predictions. The region of low $m_{\gamma\gamma}$ is sensitive to multi-jet configurations, which are only modelled at low precision in all predictions.

References

[1] CMS Collaboration, *Measurement of the production cross section for pairs of isolated photons in pp collisions at $\sqrt{s} = 7$ TeV*, JHEP **01** (2012) 133, arXiv: 1110.6461 [hep-ex] (cit. on p. 2).

[2] CMS Collaboration, *Measurement of differential cross sections for the production of a pair of isolated photons in pp collisions at $\sqrt{s} = 7$ TeV*, Eur. Phys. J. C **74** (2014) 3129, arXiv: 1405.7225 [hep-ex] (cit. on p. 2).

[3] ATLAS Collaboration, *Measurement of the isolated diphoton cross section in pp collisions at $\sqrt{s} = 7$ TeV with the ATLAS detector*, Phys. Rev. D **85** (2012) 012003, arXiv: 1107.0581 [hep-ex] (cit. on pp. 2, 8).

[4] ATLAS Collaboration, *Measurement of isolated-photon pair production in pp collisions at $\sqrt{s}$ = 7 TeV with the ATLAS detector*, JHEP **01** (2013) 086, arXiv: 1211.1913 [hep-ex] (cit. on pp. 2, 8).

[5] ATLAS Collaboration, *Measurements of integrated and differential cross sections for isolated photon pair production in pp collisions at $\sqrt{s}$ = 8 TeV with the ATLAS detector*, Phys. Rev. D **95** (2017) 112005, arXiv: 1704.03839 [hep-ex] (cit. on p. 2).

[6] CMS Collaboration, *Measurement of differential cross sections for inclusive isolated-photon and photon+jet production in proton–proton collisions at $\sqrt{s}$ = 13 TeV*, Eur. Phys. J. C **79** (2019) 20, arXiv: 1807.00782 [hep-ex] (cit. on p. 2).

[7] ATLAS Collaboration, *Measurement of the cross section for inclusive isolated-photon production in pp collisions at $\sqrt{s}$ = 13 TeV using the ATLAS detector*, Phys. Lett. B **770** (2017) 473, arXiv: 1701.06882 [hep-ex] (cit. on pp. 2, 8).

[8] ATLAS Collaboration, *Measurement of the cross section for isolated-photon plus jet production in pp collisions at $\sqrt{s}$ = 13 TeV using the ATLAS detector*, Phys. Lett. B **780** (2018) 578, arXiv: 1801.00112 [hep-ex] (cit. on pp. 2, 8).

[9] ATLAS Collaboration, *Measurement of the ratio of cross sections for inclusive isolated-photon production in pp collisions at $\sqrt{s}$ = 13 and 8 TeV with the ATLAS detector*, JHEP **04** (2019) 093, arXiv: 1901.10075 [hep-ex] (cit. on p. 2).

[10] ATLAS Collaboration, *Measurement of the inclusive isolated-photon cross section in pp collisions at $\sqrt{s}$ = 13 TeV using 36 fb^{-1} of ATLAS data*, JHEP **10** (2019) 203, arXiv: 1908.02746 [hep-ex] (cit. on pp. 2, 8).

[11] ATLAS Collaboration, *Measurement of isolated-photon plus two-jet production in pp collisions at $\sqrt{s}$ = 13 TeV with the ATLAS detector*, JHEP **03** (2020) 179, arXiv: 1912.09866 [hep-ex] (cit. on p. 2).

[12] ATLAS Collaboration, *The ATLAS Experiment at the CERN Large Hadron Collider*, JINST **3** (2008) S08003 (cit. on p. 3).

[13] ATLAS Collaboration, *Performance of the ATLAS trigger system in 2015*, Eur. Phys. J. C **77** (2017) 317, arXiv: 1611.09661 [hep-ex] (cit. on p. 3).

[14] ATLAS Collaboration, *ATLAS data quality operations and performance for 2015–2018 data-taking*, JINST **15** (2020) P04003, arXiv: 1911.04632 [physics.ins-det] (cit. on p. 3).

[15] ATLAS Collaboration, *Performance of electron and photon triggers in ATLAS during LHC Run 2*, Eur. Phys. J. C **80** (2020) 47, arXiv: 1909.00761 [hep-ex] (cit. on p. 4).

[16] S. Agostinelli et al., *GEANT4 – a simulation toolkit*, Nucl. Instrum. Meth. A **506** (2003) 250 (cit. on p. 4).

[17] E. Bothmann et al., *Event generation with Sherpa 2.2*, SciPost Phys. **7** (2019) 034, arXiv: 1905.09127 [hep-ph] (cit. on pp. 4, 5).

[18] T. Sjöstrand, S. Mrenna and P. Z. Skands, *A brief introduction to PYTHIA 8.1*, Comput. Phys. Commun. **178** (2008) 852, arXiv: 0710.3820 [hep-ph] (cit. on p. 4).

[19] T. Gleisberg and S. Höche, *Comix, a new matrix element generator*, JHEP **12** (2008) 039, arXiv: 0808.3674 [hep-ph] (cit. on p. 4).

[20] S. Schumann and F. Krauss, *A parton shower algorithm based on Catani–Seymour dipole factorisation*, JHEP **03** (2008) 038, arXiv: 0709.1027 [hep-ph] (cit. on p. 4).

[21] S. Höche, F. Krauss, M. Schönherr and F. Siegert, *A critical appraisal of NLO+PS matching methods*, JHEP **09** (2012) 049, arXiv: 1111.1220 [hep-ph] (cit. on p. 4).

[22] S. Höche, F. Krauss, M. Schönherr and F. Siegert, *QCD matrix elements + parton showers. The NLO case*, JHEP **04** (2013) 027, arXiv: 1207.5030 [hep-ph] (cit. on p. 4).

[23] F. Cascioli, P. Maierhöfer and S. Pozzorini, *Scattering Amplitudes with Open Loops*, Phys. Rev. Lett. **108** (2012) 111601, arXiv: 1111.5206 [hep-ph] (cit. on p. 4).

[24] A. Denner, S. Dittmaier and L. Hofer, *COLLIER: A fortran-based complex one-loop library in extended regularizations*, Comput. Phys. Commun. **212** (2017) 220, arXiv: 1604.06792 [hep-ph] (cit. on p. 4).

[25] R. D. Ball et al., *Parton distributions for the LHC run II*, JHEP **04** (2015) 040, arXiv: 1410.8849 [hep-ph] (cit. on pp. 4, 19).

[26] F. Siegert, *A practical guide to event generation for prompt photon production with Sherpa*, J. Phys. **G44** (2017) 044007, arXiv: 1611.07226 [hep-ph] (cit. on pp. 4, 19).

[27] S. Frixione, *Isolated photons in perturbative QCD*, Phys. Lett. **B429** (1998) 369, arXiv: hep-ph/9801442 [hep-ph] (cit. on pp. 4, 19).

[28] R. D. Ball et al., *Parton distributions with LHC data*, Nucl. Phys. B **867** (2013) 244, arXiv: 1207.1303 [hep-ph] (cit. on pp. 4, 20).

[29] ATLAS Collaboration, *ATLAS Pythia 8 tunes to 7 TeV data*, ATL-PHYS-PUB-2014-021, 2014, URL: https://cds.cern.ch/record/1966419 (cit. on p. 4).

[30] S. Alioli, P. Nason, C. Oleari and E. Re, *A general framework for implementing NLO calculations in shower Monte Carlo programs: the POWHEG BOX*, JHEP **06** (2010) 043, arXiv: 1002.2581 [hep-ph] (cit. on p. 4).

[31] P. Nason, *A new method for combining NLO QCD with shower Monte Carlo algorithms*, JHEP **11** (2004) 040, arXiv: hep-ph/0409146 (cit. on p. 4).

[32] ATLAS Collaboration, *Measurement of the Z/γ^* boson transverse momentum distribution in pp collisions at $\sqrt{s} = 7$ TeV with the ATLAS detector*, JHEP **09** (2014) 145, arXiv: 1406.3660 [hep-ex] (cit. on p. 4).

[33] N. Davidson, T. Przedzinski and Z. Was, *PHOTOS interface in C++: Technical and physics documentation*, Comput. Phys. Commun. **199** (2016) 86, arXiv: 1011.0937 [hep-ph] (cit. on p. 4).

[34] C. Anastasiou, L. J. Dixon, K. Melnikov and F. Petriello, *High precision QCD at hadron colliders: Electroweak gauge boson rapidity distributions at next-to-next-to leading order*, Phys. Rev. D **69** (2004) 094008, arXiv: hep-ph/0312266 (cit. on p. 4).

[35] ATLAS Collaboration, *Measurement of the transverse momentum distribution of Drell–Yan lepton pairs in proton–proton collisions at $\sqrt{s} = 13$ TeV with the ATLAS detector*, (2019), arXiv: 1912.02844 [hep-ex] (cit. on pp. 5, 17).

[36] ATLAS Collaboration, *Photon identification in 2015 ATLAS data*, ATL-PHYS-PUB-2016-014, 2016, URL: https://cds.cern.ch/record/2203125 (cit. on p. 5).

[37] ATLAS Collaboration, *Electron and photon energy calibration with the ATLAS detector using LHC Run 1 data*, Eur. Phys. J. C **74** (2014) 3071, arXiv: 1407.5063 [hep-ex] (cit. on p. 5).

[38] ATLAS Collaboration, *Electron and photon energy calibration with the ATLAS detector using 2015–2016 LHC proton–proton collision data*, JINST **14** (2019) P03017, arXiv: 1812.03848 [hep-ex] (cit. on pp. 5, 18).

[39] ATLAS Collaboration, *Measurement of Higgs boson production in the diphoton decay channel in pp collisions at center-of-mass energies of 7 and 8 TeV with the ATLAS detector*, Phys. Rev. D **90** (2014) 112015, arXiv: 1408.7084 [hep-ex] (cit. on p. 5).

[40] ATLAS Collaboration, *Measurement of the Higgs boson production cross section at 7, 8 and 13 TeV center-of-mass energies in the $H \to \gamma\gamma$ channel with the ATLAS detector*, ATLAS-CONF-2015-060, 2015, URL: https://cds.cern.ch/record/2114826 (cit. on p. 5).

[41] ATLAS Collaboration, *Electron and photon performance measurements with the ATLAS detector using the 2015–2017 LHC proton–proton collision data*, JINST **14** (2019) P12006, arXiv: 1908.00005 [hep-ex] (cit. on pp. 5, 10, 17).

[42] ATLAS Collaboration, *Topological cell clustering in the ATLAS calorimeters and its performance in LHC Run 1*, Eur. Phys. J. C **77** (2017) 490, arXiv: 1603.02934 [hep-ex] (cit. on p. 5).

[43] M. Cacciari, G. P. Salam and G. Soyez, *The catchment area of jets*, JHEP **04** (2008) 005, arXiv: 0802.1188 [hep-ph] (cit. on p. 6).

[44] S. D. Ellis and D. E. Soper, *Successive combination jet algorithm for hadron collisions*, Phys. Rev. D **48** (1993) 3160, arXiv: hep-ph/9305266 (cit. on p. 6).

[45] A. Banfi, S. Redford, M. Vesterinen, P. Waller and T. R. Wyatt, *Optimisation of variables for studying dilepton transverse momentum distributions at hadron colliders*, Eur. Phys. J. **C71** (2011) 1600, arXiv: 1009.1580 [hep-ex] (cit. on p. 7).

[46] ATLAS Collaboration, *Study of the spin of the Higgs-like boson in the two photon decay channel using 20.7 fb^{-1} of pp collisions collected at $\sqrt{s} = 8$ TeV with the ATLAS detector*, ATLAS-CONF-2013-029, 2013, URL: https://cds.cern.ch/record/1527124 (cit. on p. 7).

[47] ATLAS Collaboration, *Measurement of the inclusive isolated prompt photon cross section in pp collisions at $\sqrt{s} = 7$ TeV with the ATLAS detector*, Phys. Rev. D **83** (2011) 052005, arXiv: 1012.4389 [hep-ex] (cit. on p. 8).

[48] ATLAS Collaboration, *Measurement of the inclusive isolated prompt photon cross-section in pp collisions at $\sqrt{s} = 7$ TeV using 35 pb^{-1} of ATLAS data*, Phys. Lett. B **706** (2011) 150, arXiv: 1108.0253 [hep-ex] (cit. on p. 8).

[49] ATLAS Collaboration, *Measurement of the production cross section of an isolated photon associated with jets in proton–proton collisions at $\sqrt{s} = 7$ TeV with the ATLAS detector*, Phys. Rev. D **85** (2012) 092014, arXiv: 1203.3161 [hep-ex] (cit. on p. 8).

[50] ATLAS Collaboration, *Dynamics of isolated-photon plus jet production in pp collisions at $\sqrt{s} = 7$ TeV with the ATLAS detector*, Nucl. Phys. B **875** (2013) 483, arXiv: 1307.6795 [hep-ex] (cit. on p. 8).

[51] ATLAS Collaboration, *Measurement of the inclusive isolated prompt photons cross section in pp collisions at $\sqrt{s} = 7$ TeV with the ATLAS detector using 4.6 fb^{-1}*, Phys. Rev. D **89** (2014) 052004, arXiv: 1311.1440 [hep-ex] (cit. on p. 8).

[52] ATLAS Collaboration, *Measurement of the inclusive isolated prompt photon cross section in pp collisions at $\sqrt{s} = 8$ TeV with the ATLAS detector*, JHEP **08** (2016) 005, arXiv: 1605.03495 [hep-ex] (cit. on p. 8).

[53] ATLAS Collaboration, *High-E_T isolated-photon plus jets production in pp collisions at $\sqrt{s} = 8$ TeV with the ATLAS detector*, Nucl. Phys. B **918** (2017) 257, arXiv: 1611.06586 [hep-ex] (cit. on p. 8).

[54] ATLAS Collaboration, *Measurement of the photon identification efficiencies with the ATLAS detector using LHC Run 2 data collected in 2015 and 2016*, Eur. Phys. J. C **79** (2019) 205, arXiv: 1810.05087 [hep-ex] (cit. on pp. 10, 18).

[55] G. D'Agostini, *A multidimensional unfolding method based on Bayes' theorem*, Nucl. Instrum. Meth. A **362** (1995) 487 (cit. on p. 14).

[56] ATLAS Collaboration, *Luminosity determination in pp collisions at $\sqrt{s} = 13$ TeV using the ATLAS detector at the LHC*, ATLAS-CONF-2019-021, 2019, URL: https://cds.cern.ch/record/2677054 (cit. on p. 19).

[57] G. Avoni et al., *The new LUCID-2 detector for luminosity measurement and monitoring in ATLAS*, JINST **13** (2018) P07017 (cit. on p. 19).

[58] T. Gehrmann et al., *Jet cross sections and transverse momentum distributions with NNLOJET*, PoS **RADCOR2017** (2018) 074, ed. by A. Hoang and C. Schneider, arXiv: 1801.06415 [hep-ph] (cit. on p. 19).

[59] A. Gehrmann-De Ridder, T. Gehrmann and E. W. N. Glover, *Antenna subtraction at NNLO*, JHEP **09** (2005) 056, arXiv: hep-ph/0505111 (cit. on p. 19).

[60] J. Currie, E. W. N. Glover and S. Wells, *Infrared structure at NNLO using antenna subtraction*, JHEP **04** (2013) 066, arXiv: 1301.4693 [hep-ph] (cit. on p. 19).

[61] S. Dulat et al., *New parton distribution functions from a global analysis of quantum chromodynamics*, Phys. Rev. D **93** (2016) 033006, arXiv: 1506.07443 [hep-ph] (cit. on p. 19).

[62] L. A. Harland-Lang, A. D. Martin, P. Motylinski and R. S. Thorne, *Parton distributions in the LHC era: MMHT 2014 PDFs*, Eur. Phys. J. C **75** (2015) 204, arXiv: 1412.3989 [hep-ph] (cit. on p. 19).

[63] X. Chen, T. Gehrmann, N. Glover, M. Höfer and A. Huss, *Isolated photon and photon+jet production at NNLO QCD accuracy*, JHEP **04** (2020) 166, arXiv: 1904.01044 [hep-ph] (cit. on p. 19).

[64] S. Amoroso et al., 'Les Houches 2019: Physics at TeV Colliders: Standard Model Working Group Report', 11th Les Houches Workshop on Physics at TeV Colliders: PhysTeV Les Houches, 2020, arXiv: 2003.01700 [hep-ph] (cit. on p. 19).

[65] T. Binoth, J. P. Guillet, E. Pilon and M. Werlen, *A full next-to-leading order study of direct photon pair production in hadronic collisions*, Eur. Phys. J. **C16** (2000) 311, arXiv: hep-ph/9911340 [hep-ph] (cit. on p. 20).

[66] H.-L. Lai et al., *New parton distributions for collider physics*, Phys. Rev. D **82** (2010) 074024, arXiv: 1007.2241 [hep-ph] (cit. on p. 20).

[67] A. D. Martin, W. J. Stirling, R. S. Thorne and G. Watt, *Parton distributions for the LHC*, Eur. Phys. J. C **63** (2009) 189, arXiv: 0901.0002 [hep-ph] (cit. on p. 20).

Appendix

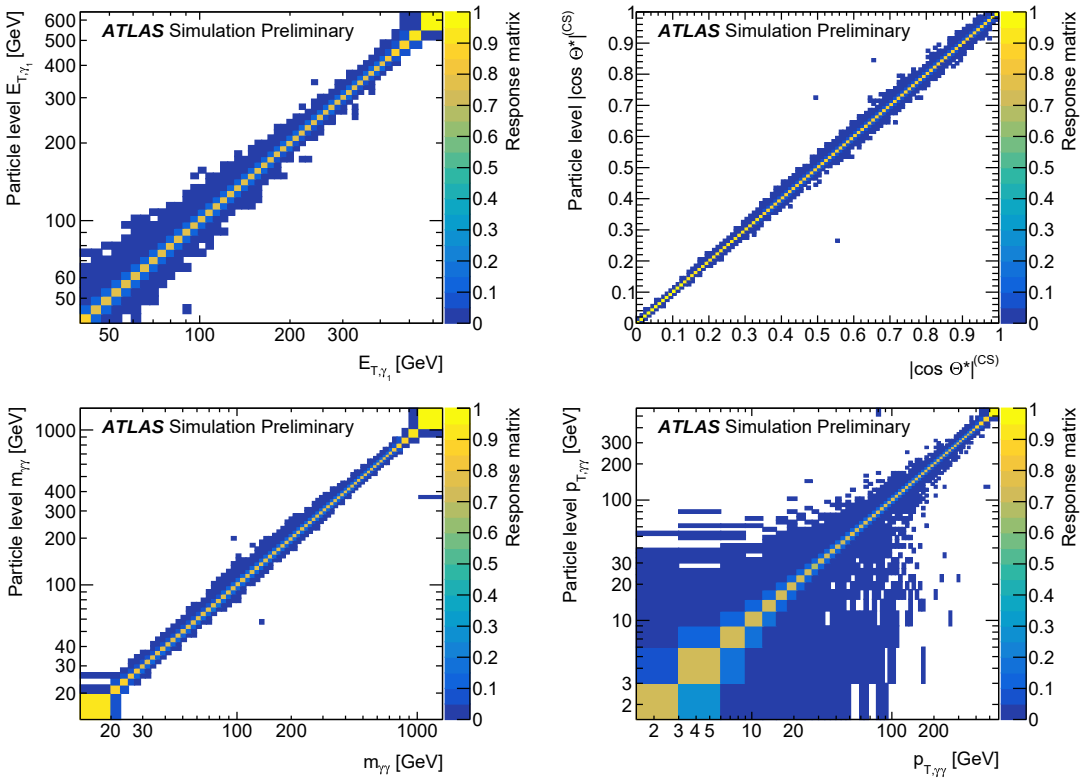

Figure 10: The response matrices extracted from the Sherpa diphoton sample for events passing the particle-level and detector-level selection for E_{T,γ_1}, $|\cos\theta^*|^{(\mathrm{CS})}$, $m_{\gamma\gamma}$ and $p_{\mathrm{T},\gamma\gamma}$ are depicted. They show the conditional probablity for an event in a given particle-level bin to be reconstructed in one of the detector-level bins. This serves as an input to the Bayesian unfolding procedure.

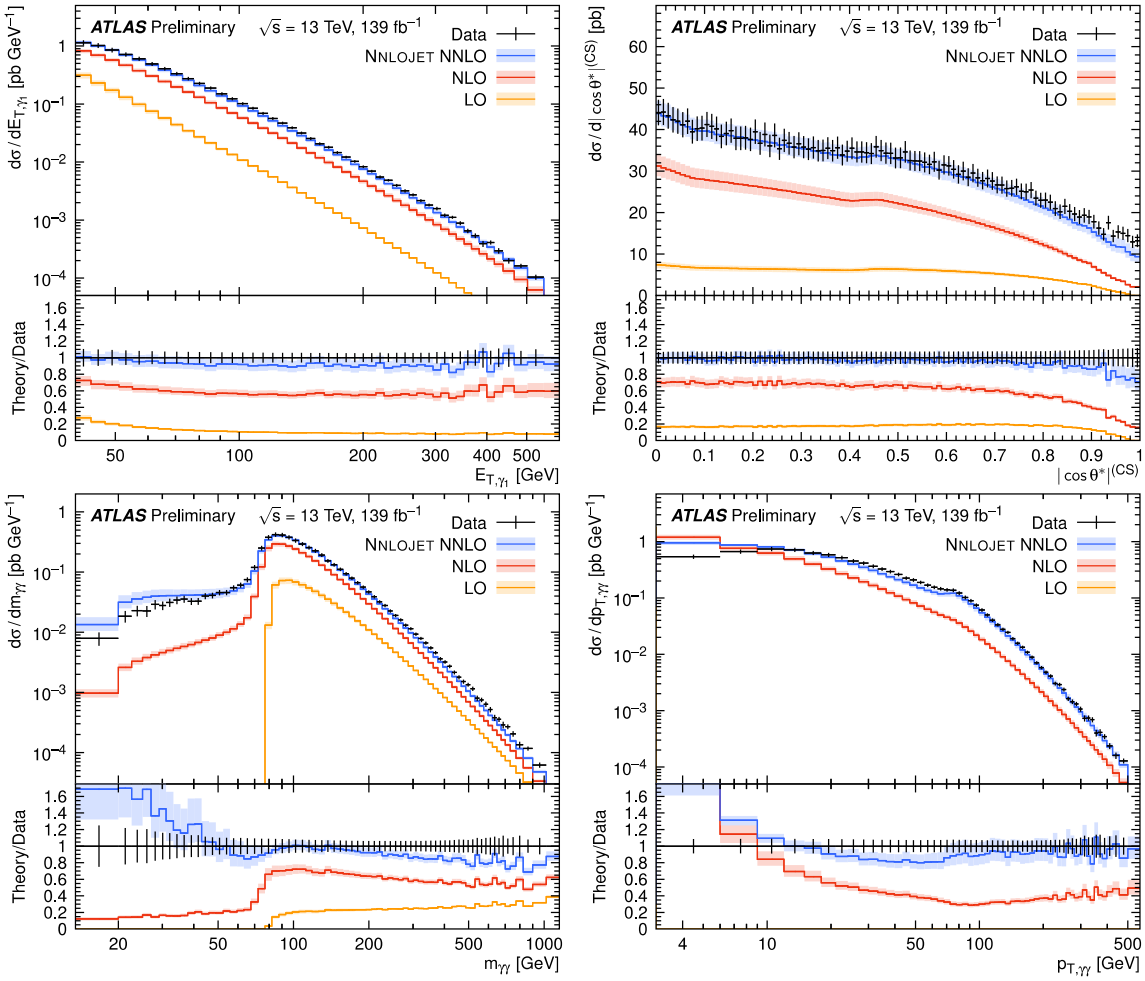

Figure 11: Comparison of the unfolded measurements with NNLOJET predictions at NNLO (blue), NLO (red) and LO (orange) accuracies differentially in E_{T,γ_1}, $|\cos\theta^*|^{(\mathrm{CS})}$, $m_{\gamma\gamma}$ and $p_{\mathrm{T},\gamma\gamma}$. The uncertainty bands represent the 7-point scale variations, while the uncertainty bars represent the statistical uncertainty of the NNLOJET predictions and the total uncertainty of the data.

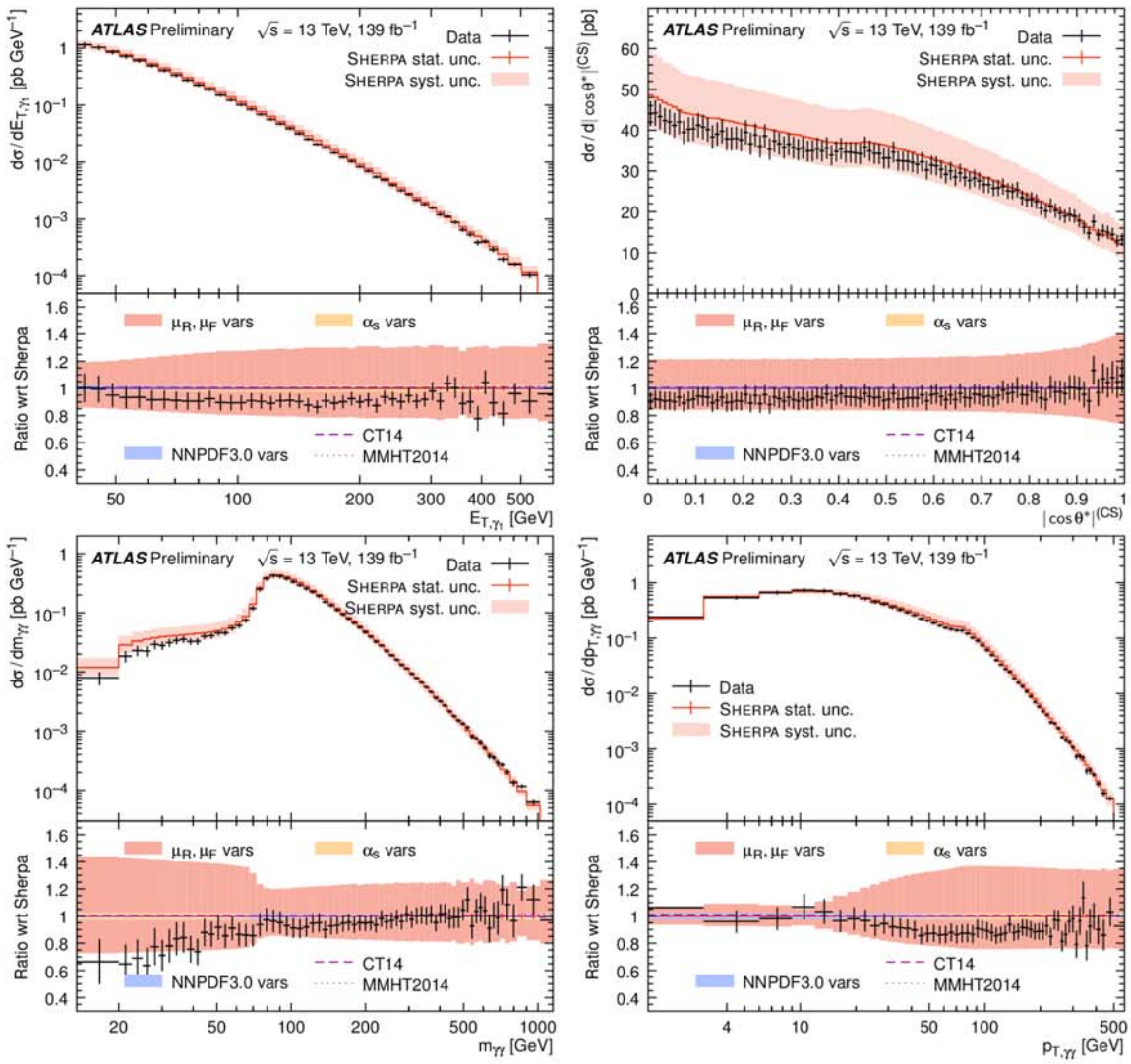

Figure 12: Comparison of the unfolded measurements with SHERPA predictions differentially in E_{T,γ_1}, $|\cos\theta^*|^{(\mathrm{CS})}$, $m_{\gamma\gamma}$ and $p_{\mathrm{T},\gamma\gamma}$. The SHERPA total systematic uncertainty (light red band in the main plot) is broken down into QCD scale variations (dark-red band), α_S variations (orange band) and PDF uncertainties (blue band) in the ratio plot. Additionally, predictions with two alternative central PDF sets are displayed for CT14 (dashed) and MMHT2014 (dotted), and are very similar to the nominal prediction. The uncertainty bars represent the statistical uncertainty of the SHERPA predictions and the total uncertainty of the data.